Statistical Analyses of Satellite Cloud Object Data from CERES. Part II: Tropical Convective Cloud Objects during 1998 El Niño and Evidence for Supporting the Fixed Anvil Temperature Hypothesis

KUAN-MAN XU, TAKMENG WONG, AND BRUCE A. WIELICKI

NASA Langley Research Center, Hampton, Virginia

LINDSAY PARKER

Science Applications International Corporation, Hampton, Virginia

BING LIN

NASA Langley Research Center, Hampton, Virginia

ZACHARY A. EITZEN

NASA Langley Research Center, and Science Applications International Corporation, Hampton, Virginia

MARK BRANSON

Colorado State University, Fort Collins, Colorado

(Manuscript received 21 November 2005, in final form 9 August 2006)

ABSTRACT

Characteristics of tropical deep convective cloud objects observed over the tropical Pacific during January–August 1998 are examined using the Tropical Rainfall Measuring Mission/Clouds and the Earth's Radiant Energy System Single Scanner Footprint (SSF) data. These characteristics include the frequencies of occurrence and statistical distributions of cloud physical properties. Their variations with cloud object size, sea surface temperature (SST), and satellite precession cycle are analyzed in detail. A cloud object is defined as a contiguous patch of the earth composed of satellite footprints within a single dominant cloud-system type.

It is found that statistical distributions of cloud physical properties are significantly different among three size categories of cloud objects with equivalent diameters of 100–150 (small), 150–300 (medium), and >300 km (large), except for the distributions of ice particle size. The distributions for the larger-size category of cloud objects are more skewed toward high SSTs, high cloud tops, low cloud-top temperature, large ice water path, high cloud optical depth, low outgoing longwave (LW) radiation, and high albedo than the smaller-size category. As SST varied from one satellite precession cycle to another, the changes in macrophysical properties of cloud objects over the entire tropical Pacific were small for the large-size category of cloud objects, relative to those of the small- and medium-size categories. This evidence supports the fixed anvil temperature hypothesis of Hartmann and Larson for the large-size category. Combined with the result that a higher percentage of the large-size category of cloud objects occurs during higher SST subperiods, this implies that macrophysical properties of cloud objects would be less sensitive to further warming of the climate. On the other hand, when cloud objects are classified according to SST ranges, statistical characteristics of cloud microphysical properties, optical depth, and albedo are not sensitive to the SST, but those of cloud macrophysical properties are dependent upon the SST. This result is related to larger differences in large-scale dynamics among the SST ranges than among the satellite precession cycles. Frequency distributions of vertical velocity from the European Centre for Medium-Range Weather Forecasts model that is matched to each cloud object are used to further understand some of the findings in this study.

Corresponding author address: Dr. Kuan-Man Xu, Climate Science Branch, NASA Langley Research Center, Mail Stop 420, Hampton, VA 23681.
E-mail: Kuan-Man.Xu@nasa.gov

DOI: 10.1175/JCLI4069.1

1. Introduction

Climate model simulations are usually validated against gridded monthly mean satellite observations. Numerical weather forecasts are validated against surface and upper-air observations, at least, at the daily time scale. In both types of validations, the gridded data are used. They represent averages of physical parameters over an area of hundreds of kilometers in a horizontal direction. In the validation of climate model simulations, monthly mean gridded satellite data may include many different types of cloud systems, due to changes in large-scale dynamic and thermodynamic environments. While these monthly averaged satellite data are useful in some climate applications, they do not sufficiently constrain critical assumptions about the treatment of subgrid-scale processes and thus are generally not suitable to fully explore the direct cause of model deficiencies or to directly improve physical parameterizations of climate models. Even when such data are carefully examined against model simulations, the models may perform well for the wrong reasons due to cancellation of errors in the monthly averaged model output.

Xu et al. (2005, hereafter Part I) recently proposed a new methodology to analyze statistical properties of cloud systems from Earth Observing System (EOS) satellites in order to more rigorously validate model simulations. This is termed the "cloud object" approach. This approach identifies a cloud object as a contiguous patch of the earth composed of satellite footprints within a single dominant cloud-system type. The shape and size of a cloud object are determined by the satellite footprint data and by the selection criteria based upon cloud physical properties for a given cloud-system type. For example, deep convective cloud objects are identified with footprints that have a cloud optical depth (τ) greater than 10, cloud-top height greater than 10 km, and cloud fraction of 100%. No arbitrary grid cell of the earth is used in this new methodology. It is therefore *not* an Eulerian approach as in the monthly averaged satellite data.

As explained in Part I, this new approach to satellite data analysis includes the following three major steps. First, individual cloud objects are selected from the large volume of satellite footprint data that contain the selected cloud object type. Second, large ensembles of cloud objects are combined to generate statistically robust cloud physical characteristics to reach climate accuracy (Ohring et al. 2005) for different cloud-system types. Statistical properties of cloud objects are analyzed in terms of the summary probability density functions (pdfs) or histograms over an ensemble of cloud objects, that is, the combined pdfs of individual cloud objects, instead of the simple averages and standard deviations. Third, the atmospheric state is matched to the time and location of each cloud object in such a way to allow for stratification of observed cloud objects according to some independent measures of the atmospheric states. As explained below, this is needed to derive the partial derivatives of cloud properties versus atmospheric states, or the individual components of cloud feedbacks. These atmospheric states can be represented by the sea surface temperature (SST), the vertical velocity at 500 hPa for tropical deep convective cloud objects, or the static stability in the lower troposphere for boundary layer cloud objects.

Based upon linear systems analysis, Schlesinger (1985) defined climate feedbacks including cloud–climate feedbacks in terms of partial derivatives that represent the rates of response of internal variables to changes in external forcings. The feedback strength is decomposed into individual feedback strengths by assuming that the feedbacks are both independent of each other and linear in nature. Obviously, nonlinearities inherent in cloud–radiation processes distort the analyzed feedbacks in this linear analysis framework. The cloud object approach has the potential to greatly simplify the understanding of cloud–climate feedback processes because the data are not composite averages of very different types of cloud systems. The changes in the feedback strengths are then a combination of the changes in the frequency of occurrence of each individual cloud-system type and the changes in cloud physical and radiative properties of the same cloud-system type. This is analogous to the separation of cloud property changes into dynamic and thermodynamic components proposed by Bony et al. (2004).

The cloud object data can be used to provide observational evidence for supporting hypotheses for climate change. There are several hypotheses regarding tropical climate change, which postulate that relationships exist between radiative properties and SSTs. Ramanathan and Collins (1991) analyzed the monthly mean Earth Radiation Budget Experiment (ERBE; Barkstrom et al. 1989) data and proposed a cirrus cloud thermostat hypothesis. This hypothesis suggested that the high albedos of tropical deep convective clouds can limit the upper bound on the SST. Lindzen et al. (2001) proposed an adaptive iris hypothesis in which the tropical upper-tropospheric anvils act as a strong negative feedback on the global climate system. Both hypotheses have been disputed by many studies (e.g., Lau et al. 1994; Hartmann and Michelsen 1993, 2002; Lin et al. 2002, 2006; Fu et al. 2002). For both hypotheses, the radiative feedback of clouds on the energy balance is

directly related to the change of SST without considering the large-scale circulations that result from the meridional gradient of the SST (e.g., Hartmann and Michelsen 1993; Larson and Hartmann 2003b).

It is well known that the subsidence region of the Tropics is required to close the mass budget and the decrease of albedos in the subsidence region can cancel out the albedo increases over convective regions as the mean SST increases in the Tropics. This means that there exists an approximate heat balance in the tropical troposphere between the radiative cooling in the subsidence region and convective heating by latent heat release in the convective regions. Hartmann and Larson (2002) proposed the fixed anvil temperature (FAT) hypothesis in which the emission temperature at the top of convective anvil clouds in the Tropics will remain constant during climate change. They based this on the fact that the radiative cooling at the top of convective anvil clouds is determined by the emission temperature due to inefficient radiative emission from water vapor through the Clausius–Clapeyron relationship. This hypothesis was supported by mesoscale numerical model simulations (Larson and Hartmann 2003a,b) and recently by cloud-resolving model simulations (Kuang and Hartmann 2007), but it has not been observationally confirmed. The use of cloud object data represents the first attempt to provide evidence for supporting this hypothesis.

In the present part of this series of studies, statistical characteristics of tropical convective cloud objects (hereafter "cloud objects") will be analyzed from January to August 1998 of Tropical Rainfall Measuring Mission (TRMM)/Clouds and the Earth's Radiant Energy System (CERES) data period. This period corresponds to the mature and dissipative phases of the 1997/98 El Niño. The objectives of this study are threefold: 1) to contrast the differences among three size categories of cloud objects, 2) to explore the relationships of the statistical properties of cloud objects with atmospheric state variables, such as SST and vertical velocity, and 3) to provide evidence for supporting the FAT hypothesis of Hartmann and Larson (2002). Part I of this series of study presented some preliminary results from the analysis of the statistical properties of cloud objects associated with the strong 1997/98 El Niño in March 1998 and the very weak 2000 La Niña in March 2000. The present part extends the analysis of Part I to a longer period and to a greater depth.

Section 2 briefly describes satellite data and cloud object methodology. Results for the variations of cloud object characteristics with size, SST, and satellite precession cycle are presented in sections 3, 4, and 5, respectively. Conclusions and discussion are given in section 6.

2. Data and methodology

a. Cloud object data

The details of cloud object methodology and the data used in generating the cloud object data product are presented in Part I. Briefly, the basic data with which the cloud object data are produced are a level-2 CERES Single Scanner Footprint (SSF) top-of-atmosphere (TOA)/Surface Fluxes and Clouds data product (Wielicki et al. 1996). The cloud object data product contains cloud optical, microphysical, and macrophysical properties and broadband TOA reflected shortwave (SW) and emitted longwave (LW) fluxes from the CERES instrument. The full list of these parameters is given in Table 1 of Part I. The CERES broadband radiative fluxes are produced using the new generation of angular distribution models derived from the TRMM/CERES broadband radiance observations (Loeb et al. 2003). Scene identification (type and clear/cloudy) and cloud properties (i.e., cloud effective height, temperature, pressure, particle types, and equivalent diameters) are retrieved from the high-resolution cloud imager, the Visible Infrared Scanner (VIRS), on the TRMM satellite. These data have been averaged over the larger CERES instrument footprints to produce an integrated and radiation-constrained cloud and radiation dataset. Details of the retrieval methods are described in Minnis et al. (1997).

b. Cloud object methodology

A cloud object is defined as a contiguous patch composed of CERES footprints that satisfy a set of physically based cloud-system selection criteria. A "region growing" strategy based on imager-derived cloud properties is used to identify the cloud objects within a single satellite swath (Wielicki and Welch 1986). For all CERES footprints in a 700-km-wide TRMM swath, each CERES footprint that meets the selection criteria is marked as part of a cloud object. These "seed points" are grown using the algorithm described in Wielicki and Welch (1986). Only footprints that are adjacent and that meet the selection criteria of a single cloud type can be joined in a cloud object. By adjacent, we mean CERES footprints that are next to each other along the scanning direction or perpendicular to it. Cloud objects are uniquely determined when they share no adjacent CERES footprints. Cloud objects that grow to an equivalent diameter of less than 100 km, approximately 75 footprints, are ignored in the present analysis to limit data noise. A constant value of 100 km^2 is used for the

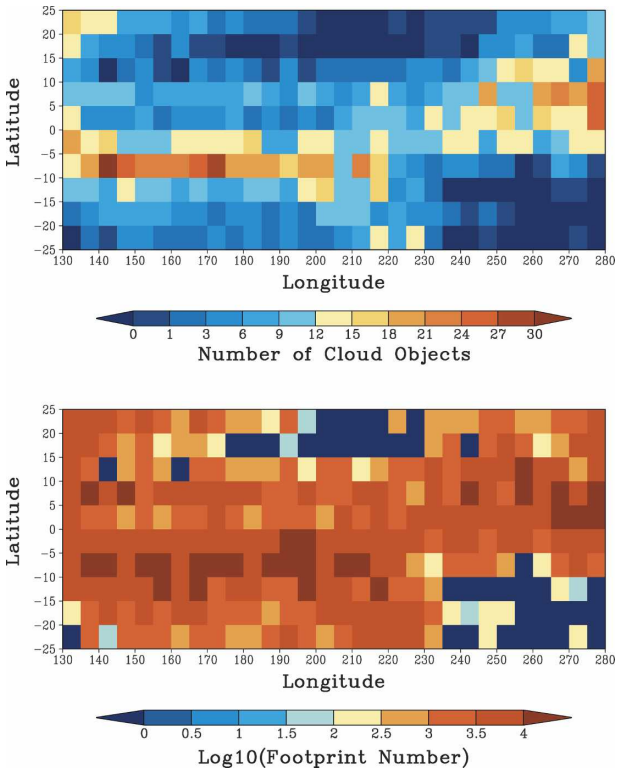

FIG. 1. (top) Number of cloud objects with equivalent diameters greater than 100 km observed in 5° × 5° areas during January–August 1998. (bottom) Base 10 logarithm of the number of satellite footprints in 5° × 5° areas for the same cloud objects shown in the top.

area of each CERES footprint to calculate the cloud object equivalent diameter. This can cause one-sigma noise in cloud object diameter of roughly 20% since the footprints have variable sizes. Further details can be found in Part I.

The selection criteria for the tropical deep convective cloud object type, as mentioned in section 1, are composed of both cloud-top height and τ because we are interested in thick, upper-tropospheric anvils and cumulonimbus towers in the Tropics. The cloud-top height must be greater than 10 km and τ must be greater than 10. The cloud fraction of the footprint must be 100%. Furthermore, all footprints must be located within the Pacific Ocean between 25°S and 25°N.

c. Data period and analysis strategy

In the present study, 8 months (January–August 1998) of the TRMM/CERES data are analyzed. These 8 months correspond to the peak and dissipative phases of the 1997/98 El Niño (Cess et al. 2001). The numbers of cloud objects and footprints in 5° × 5° areas are shown in Fig. 1 for all cloud objects with equivalent diameters greater than 100 km. The total number of cloud objects is 2257 while the total number of footprints is 1.175 million. (The cloud object data are available at http://cloud-object.larc.nasa.gov/.) As seen from Fig. 1, cloud objects occur mainly to the south of the equator in the central and western Pacific and to the north of the equator in the eastern Pacific. There are few cloud objects observed in the central Pacific between 15° and 25°N and in the eastern Pacific between 10° and 25°S.

In the analyses presented below, satellite cloud object data for this period are then sorted either by the size of cloud objects as measured by their equivalent diameter, by the (cloud object) mean SST, or by the satellite precession cycle. The mean SST is averaged from the Reynolds SST (Reynolds and Smith 1994) and interpolated to CERES footprints. The TRMM 46-day precession cycle gives a complete sampling of the diurnal cycle at a given location, that is, to avoid diurnal aliasing issues. To eliminate any impact of extratropical cloud systems on the results, a suitable measure of the baroclinicity is used in this study, which is the Eady growth rate maximum, $\sigma_{\rm BI} = 0.31 f N^{-1} \partial|\mathbf{v}|/\partial z$, where f is the Coriolis parameter, N the Brunt–Väisälä frequency, $\mathbf{v}$ the horizontal wind, and z the vertical height. This measure has been used to identify midlatitude cyclone activity (e.g., Geng and Sugi 2001; Solman and Menéndez 2002). The wind shear between 1000 and 700 hPa is computed. Any cloud object with $\sigma_{\rm BI} > 0.1$ day^{-1} is eliminated if its center is located outside the latitudinal band between 15°S and 15°N. This procedure only eliminates 6.4% (145/2257) of cloud objects plotted in Fig. 1a. In all analyses presented in sections 3–5, both the frequencies of occurrence of the remaining tropical cloud objects and the statistical distributions of cloud physical properties will be examined, as well as the frequency distributions of vertical velocity from the European Centre for Medium-Range Weather Forecasts (ECMWF) model that is matched to each cloud object.

d. Matched ECMWF data

The ECMWF analyses over the Tropics are available on 0.5625° × 0.5625° grid meshes every 6 h from its data assimilation system. The data include horizontal wind components, temperature and water vapor profiles, etc. However, the vertical velocity (in pressure coordinates ω) was not available from the ECMWF analyses. In this study, vertical velocity and advective heat and moisture tendencies are actually calculated by the Colorado State University general circulation model (GCM). The dynamic core of the GCM is run for a single time step with initial input data from ECMWF. That is, no physical parameterization in the GCM is involved in the calculation. Details of this procedure can be found in

Eitzen and Xu (2005). These tendencies are matched to the time and location of the observed cloud objects. The gap in time matching is less than 3 h. In matching the location of the cloud object, a rectangular box (latitude × longitude) is drawn to cover the four outermost corner footprints of the cloud object; that is, parts of the environment surrounding the cloud objects are included, which can be associated with positive ω. If one side of this box is larger than 7.3125° in length (13 grid cells), a maximum length of 7.3125° centered on the center of the cloud object is used instead. This happens for a few very large cloud objects or irregularly shaped cloud objects. Then, every grid cell (0.5625° × 0.5625° size) within the rectangular box will be used to calculate the frequency distributions of vertical velocity as a function of pressure, as shown in sections 3, 4, and 5.

It is well known that large-scale advective tendencies of heat and moisture are closely linked to the intensity of convective cloud systems. Because horizontal advective tendencies in the Tropics are usually small, compared to their vertical counterparts, vertical velocity can be used as an indicator of the intensity of tropical deep convection. For example, Bony et al. (2004) sorted the monthly mean TOA longwave and shortwave cloud radiative forcings at 4° × 5° grid cells according to the similarly averaged ω at 500 hPa (hereafter ω_{500}). The frequency distribution of ω_{500} in the current study shown later in the paper, however, have different characteristics because these vertical velocities are the instantaneous values at a much smaller grid cell size. In particular, the magnitudes can be 10–100 times larger than those of the monthly mean vertical velocity. Because of this instantaneousness, the frequency distributions of vertical velocity at a single level may not be able to characterize the different dynamic environments of cloud objects of different size categories, SST ranges, or precession cycles. To overcome this problem, the frequency distributions of vertical velocity are first calculated as a function of pressure for every size category. These frequency distributions are then used to calculate the frequency departures for subsets of cloud objects classified according to SST or satellite precession cycle.

3. Variations of cloud object characteristics with size

a. Frequency of occurrence

The cloud objects identified from the CERES SSF data are tabulated according to the range of their equivalent diameters. Three size categories are considered. They are defined by the ranges of 100–150 (small size), 150–300 (medium size), and greater than 300 km (large size). For convenience, they are termed the S-, M-, and L-size categories, respectively. Each category of cloud objects is evenly distributed among the western, central, and eastern Pacific regions (Table 1). The total number for the S, M, and L categories is 791, 845, and 476, respectively. Although the S- and M-size categories of cloud objects occur more frequently than the L-size category, the total numbers of CERES footprints for the L-size category are much greater, 65.9% of the sum of all three size categories, than the S- and M-size categories, due to the much larger mean number of footprints for the L-size cloud objects. The numbers of CERES footprints also vary from one cloud object to another within each size category. Table 2 shows the statistics of the footprint numbers for the S-, M-, and L-size categories. The intracategory variability is large for the L-size category because the equivalent radii range from 300 to 900 km in this size category.

TABLE 1. Number of tropical deep convective cloud objects according to different size categories and geographic regions for the January–August 1998 period.

Size category	Western Pacific (130°E–180°)	Central Pacific (180°–130°W)	Eastern Pacific (130°–80°W)
Small	307	235	249
Medium	319	255	272
Large	184	154	138
Total	810	644	659

b. Statistical properties of cloud objects

Before discussing the distributions of various cloud and radiative properties, it should be pointed out that there are many types of uncertainties (e.g., random, systematic, or caused by physical assumptions in retrieval algorithms) in remotely sensed data products (Wielicki et al. 1995). For example, uncertainties in ice particle shape can cause errors in retrievals of ice cloud optical depth, particle size, and ice water path (IWP). Uncertainties in the vertical distribution of ice particle size can cause uncertainties in both particle size and ice water path. These various types of uncertainties present a challenge to understanding the relationships of cloud and atmospheric dynamics, the same as uncertainties in atmospheric state. This is especially true for any small

TABLE 2. Statistics of the footprint numbers for small-, medium- and large-size categories of cloud objects.

Size category	Mean	Median	Standard deviation	Min	Max
Small	114	110	28	76	170
Medium	345	312	140	171	681
Large	1549	1238	911	686	7554

set of cloud observations such as might be examined in a short field experiment. The current study attempts to partially overcome these uncertainties by focusing on relationships derived from frequency distributions of very large samples of both clouds and atmospheric state. Nevertheless, it is critical to estimate and consider the impact of such errors. The appendix provides estimates of the uncertainties for the satellite-derived radiative fluxes and cloud properties used in this study. It also estimates the effect of these uncertainties on the conclusions. Overall, the range of cloud and radiative flux variations in the frequency distributions far exceed the instantaneous uncertainties, as well as the systematic biases. Tests adding such errors to the distributions conclude that the statistical results presented here are robust to these errors.

Figure 2 shows summary histograms of seven cloud, optical, and radiative properties, as well as SST, for all three size categories. These summary histograms are constructed by utilizing all 90 400, 291 800, and 737 400 footprints for the S-, M-, and L-size categories, respectively. The probability density is the number of footprints within a bin interval divided by the total number of footprints of a size category and the bin size. There are significant differences among the three size categories for all summary histograms of cloud and radiative properties, except for those of ice particle size between the S- and M-size categories and between the S- and L-size categories, despite the relatively small differences in their SST histograms (Fig. 2a). This suggests that the SST is not the primary cause for the differences in cloud, optical, and radiative properties among the three size categories, especially between the S- and M-size categories.

The differences in the SST distributions between the S- and M-size categories are not statistically significant, according to a statistical significance test based on the bootstrap method (Efron and Tibshirani 1993). The detailed procedure for this test was presented in Xu (2006). Table 3 shows the statistical significance level (p) or p value. The threshold p value is customarily chosen to be 0.05. That is, there is 95% confidence that the two pdfs are significantly different. When the p value is less than 0.05, there is a small probability that two summary histograms are formed from statistically similar cloud object populations. For example, the statistical significance test shows that the differences in SST between the S- and M-size categories are statistically insignificant with a p value greater than 0.05. The L-size cloud objects occur more frequently over relatively warmer SSTs, particularly, over SSTs between 302.0 and 303.5 K (Fig. 2a). Their SST distribution is statistically different from that of either the S- or the M-size category (Table 3).

For the type of cloud objects discussed in this study, both cloud optical depth and cloud height are cut off at 10 and 10 km, respectively (Figs. 2d,h). Although there are abrupt cutoffs in the histograms of other parameters for individual cloud objects, there are no abrupt cutoffs in the summary histograms since cutoff values differ among individual cloud objects. The lower bound in TOA albedo (Fig. 2c) and the upper bounds in outgoing longwave radiation (OLR) fluxes (Fig. 2e) and cloud-top temperature (Fig. 2b) are related to the cutoffs in cloud optical depth and cloud height, respectively.

While the ranges of the TOA albedo distributions are identical among the three size categories, the albedo distributions are slightly positively skewed for the S-size category but slightly negatively skewed for the M- and L-size categories (Fig. 2c). The modes of the distributions also differ by 0.1 between the S- and L-size categories. This difference is significant when compared to the range of the distributions, which has a value of 0.45 for this type of cloud object. Statistical significance tests also indicate that the three distributions of TOA albedos are different from each other (Table 3).

The upper limits of OLR are nearly identical ($\sim$175 W m^{-2}) for the three size categories (Fig. 2b) because of the thresholds used in identifying the cloud objects. The OLR distributions become more positively skewed as the size of cloud objects increases. This is closely related to the significant increase of cloud heights as the size of cloud objects increases (Fig. 2d). The modes of the cloud-height distributions differ by 1.5 km between the S- and L-size categories. These differences are also reflected by those in the cloud-top temperature (Fig. 2e), whose modes of the distributions between the S- and L-size categories differ by more than 10 K. These differences in cloud macrophysical properties are all consistent with the differences shown in OLR. Each of these three parameters is statistically different among the three size categories (Table 3).

There are two modes in the OLR distributions with values of 124 and 140 W m^{-2}, in particular, for the S- and M-size categories (Fig. 2b). The secondary mode does not appear in the distributions of cloud-top temperature because its bin interval is too large compared to that of OLR (see appendix). There are three closely related interpretations for this feature. First, the abundance of thick anvil clouds in larger-size categories may be associated with the 124 W m^{-2} mode, while the presence of weak convective updrafts or relatively thin anvils in the smaller-size categories may be responsible

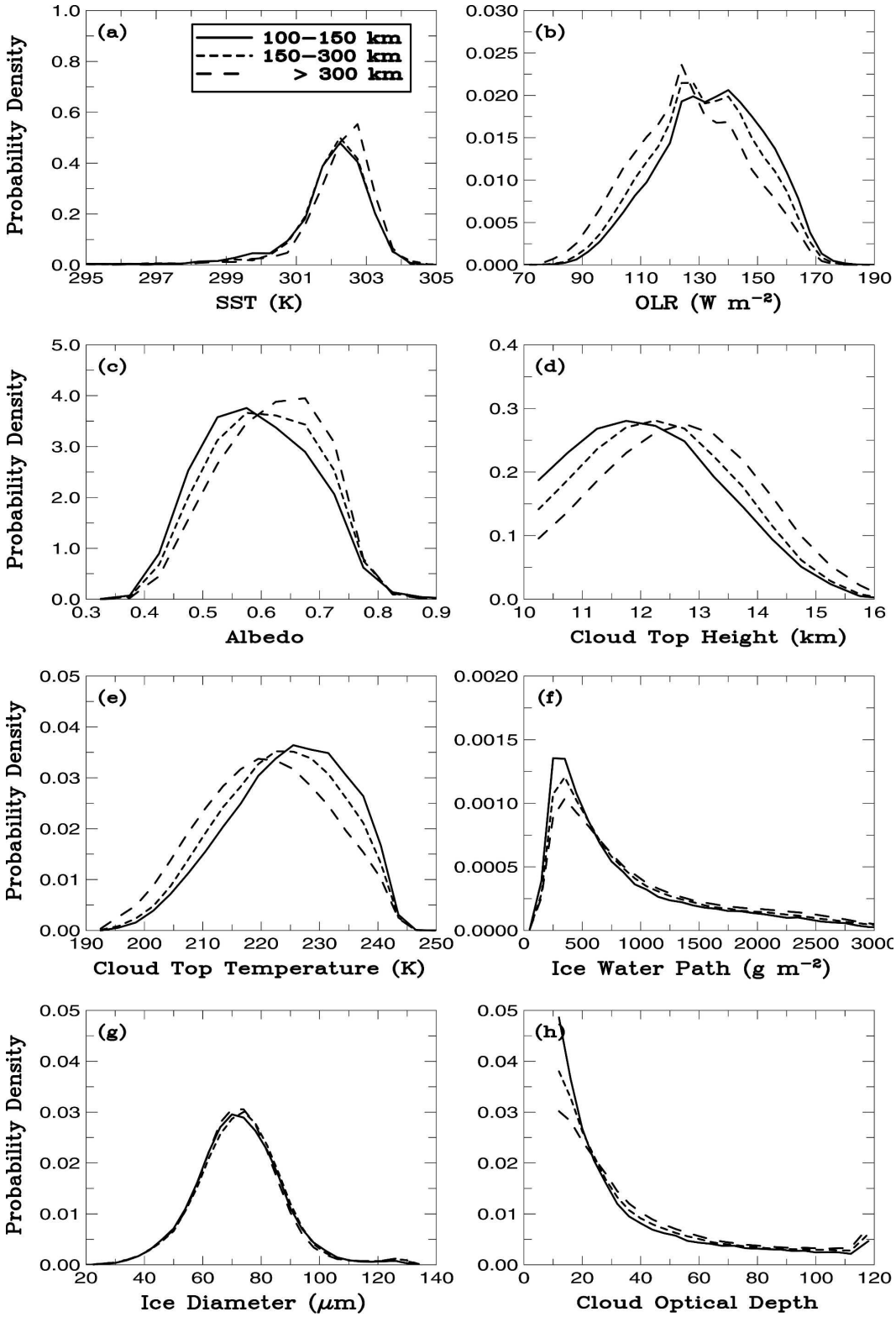

FIG. 2. Summary histograms of (a) sea surface temperature, (b) outgoing longwave radiation, (c) top-of-the-atmosphere albedo, (d) cloud-top height, (e) cloud-top temperature, (f) ice water path, (g) ice particle size, and (h) cloud optical depth of tropical convective cloud objects for the January–August 1998 period. Small-, medium-, and large-size categories of cloud objects are shown in solid, short-dashed, and long-dashed lines, respectively.

TABLE 3. The statistical significance levels or p values between a pair of size categories for different parameters of tropical convective cloud objects. Values below 0.05 are in bold and indicate statistically significant differences between two size categories, or at least 95% confidence that the two size categories are significantly different.

	Pairs of size categories		
Parameter	Small, medium	Medium, large	Small, large
SST	0.840	**<0.001**	**<0.001**
OLR	**<0.001**	**<0.001**	**<0.001**
Albedo	**<0.001**	**<0.001**	**<0.001**
Cloud height	**<0.001**	**<0.001**	**<0.001**
Cloud temperature	**<0.001**	**<0.001**	**<0.001**
Ice water path	**<0.001**	**<0.001**	**<0.001**
Ice particle size	0.331	**0.044**	0.330
Optical depth	**<0.001**	**<0.001**	**<0.001**

for the 140 W m^{-2} mode. This bimodal feature is also present in the other periods of analyzed data (Xu et al. 2005) but is most pronounced in the smaller-size categories. Second, the truncation of large, strong convective systems that are located at the edge of the narrow satellite swaths allows the coexistence of both the strong and the weak convective systems in the S- and M-size categories of cloud objects. Third, the bimodality in the OLR distributions can be associated with the diurnal variation of tropical deep convection (e.g., Gray and Jacobson 1977; Xu and Randall 1995) because the TRMM precessing orbits allow the sampling of this diurnal variation. A supporting piece of evidence for this interpretation is the lack of this bimodal feature for any of the three size categories in the OLR distribution from the sun-synchronously orbiting *Terra* satellite during March 2000 (not shown).

The differences in cloud microphysical and optical properties among the three size categories appear to be smaller than those of cloud macrophysical and radiative properties (Figs. 2f–h). In particular, ice particle sizes do not show any statistically significant differences between the S- and M-size categories or between the S- and L-size categories according to the bootstrap tests (Table 3). For all three size categories, the distributions of IWP and τ are lognormal and exponential in character, respectively (Figs. 2f,h), but there are differences with respect to how sharply the different curves fall from their maxima at the lowest few bins in τ distributions and from the peak at 350 g km^{-2} in IWP distributions. For the smaller-size categories, the probability densities in the higher values of IWP (>650 g m^{-2}) and τ (>25) are only slightly different. These differences in both IWP and τ may suggest that cumulonimbi and thick anvil clouds are more abundant in the larger-size categories. They also suggest that relatively thin anvils or weak updrafts occur more frequently within the S-size cloud objects. These are important results. Further discussion of these results is warranted.

There are several physical explanations why the statistical properties of cloud objects can be different among the three size categories of cloud objects. First, the larger cloud objects are associated with stronger convective systems so that both cumulonimbi and thick anvils penetrate much closer to the tropopause. These characteristics favor large values of IWP, τ, cloud-top height, and smaller OLR and higher TOA albedo, etc. Second, weaker convective systems or large loosely organized cloud clusters are broken into several small cloud objects because of the requirement that patch of footprints that satisfy the selection criteria must be contiguous. Thus, it is likely that these weaker systems/clusters are a major contributor to the S- or M-size cloud objects. Their characteristics are more frequently associated with small values of IWP, τ, cloud-top height, TOA albedo, and large values of OLR, etc. Third, the smaller cloud objects may result from truncation of large cloud systems by the narrow satellite swaths because some cloud systems are located near the edges of the swaths. If all S-size cloud objects result from this truncation, the statistical properties are expected to be similar to those of the L-size cloud objects. This is certainly not the case according to the results shown in Fig. 2. However, there are lower probability densities of the extreme (high or low, depending upon parameters) values in the distributions of the S-size category that are comparable to those in the L-size category, suggesting that some of the large convective cloud systems are indeed truncated by satellite swaths. This point will become clearer in section 4 when all three size categories are further classified according to SST ranges. Finally, the possibility that the differences in the pdfs among the size categories are due to differences in their geographic locations can be eliminated because the different categories of cloud objects are evenly distributed among the western, central, and eastern Pacific regions (Table 1).

c. Linkage with large-scale dynamics

Figures 3a–c show the frequency diagrams of ω as a function of pressure for the L-, M-, and S-size categories, respectively. The bin size for generating the ω frequency is 20 hPa day^{-1}. The layer thickness is 30 hPa. The number of ECMWF grid cells used in calculating the ω frequencies is 13 721, 32 419, and 53 069 for the S-, M-, and L-size categories, respectively. Many of these cells have positive ω, representing the compensating subsidence regions of the cloud systems. It was assumed in the previous section that stronger convec-

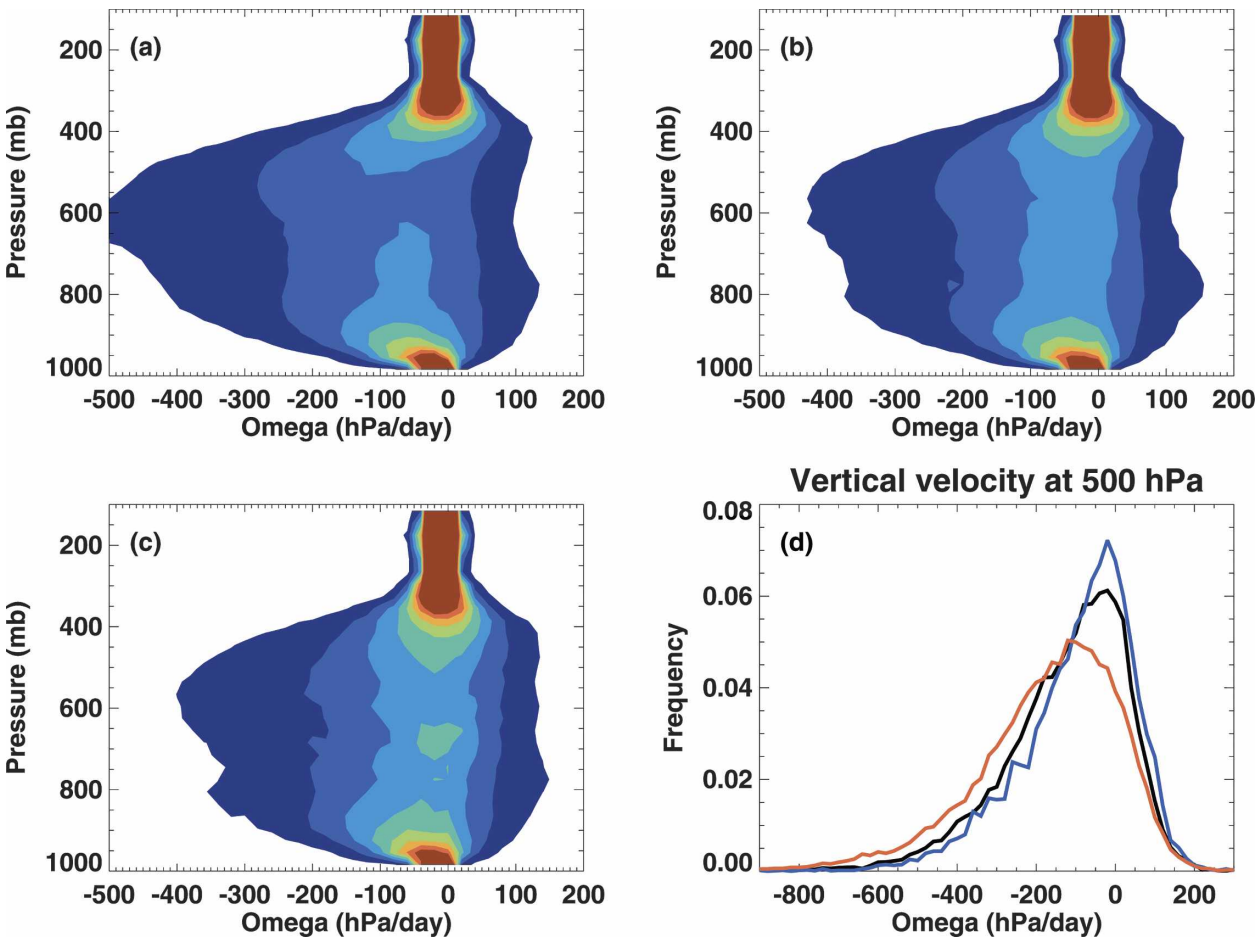

FIG. 3. Frequency diagrams of vertical velocity as a function of pressure for (a) large-, (b) medium-, and (c) small-size categories of cloud objects. The bin size is 20 hPa day^{-1}. The values corresponding to different shading areas from blue to brown areas are 0.01, 0.03, 0.05, 0.07, 0.09, 0.13, and 0.15. (d) The frequency diagram of ω_{500} for the large- (red), medium- (black), and small-size (blue) categories of cloud objects.

tive systems can be associated with larger-size cloud objects. This is confirmed by Fig. 3. The vertical velocity frequency for the L-size category is higher for large magnitudes of negative ω and lower for the ω range between -150 and $+100$ hPa day^{-1} than those of the S- and M-size categories. Similarities among the three size categories appearing in Figs. 3a–c are 1) the level at which the frequencies have the greatest range of ω is around 600 hPa, which corresponds to the level of the maximum upward motion, and 2) there is a smaller spread in ω above 300 hPa than below 900 hPa.

The differences in the frequency distributions among the three size categories can be more readily seen from the frequencies of ω_{500} (Fig. 3d). Figure 3d shows both the larger negative skewness of the distributions and the shifting of the modes of the distributions toward more negative ω_{500} for larger-size categories. The differences are large at nearly all vertical levels among the three size categories over the entire ω range except for very large positive ω (Figs. 3a–c). Although the frequency distributions below 900 and above 450 hPa are concentrated between -100 and $+50$ hPa day^{-1}, it is seen that the larger negative skewness of the distributions appears in the larger-size category. The large upward motion below 900 hPa favors intense convection while the strong upward motion above 450 hPa increases the depth and thickness of anvil clouds. Both factors are consistent with the statistical results shown in Fig. 2.

4. Variations of cloud object characteristics with SST

a. Frequency of occurrence

Table 4 shows the number of cloud objects in five SST ranges for the three size categories during January–August 1998. The mean SST associated with each cloud object is used to determine which SST range a

TABLE 4. Number of cloud objects for small-, medium-, and large-size categories as a function of SST ranges. The ratios of large size to all sizes are also shown for the number of cloud objects [ratio (number)] and the total number of footprints [ratio (footprint)].

Size category	301.25 K	301.75 K	302.25 K	302.75 K	303.25 K
Small	181	155	189	160	106
Medium	176	163	215	180	111
Large	71	87	122	136	60
Total	428	405	526	476	277
Ratio (number)	0.166	0.215	0.232	0.286	0.217
Ratio (footprint)	0.546	0.631	0.668	0.736	0.666

cloud object belongs to. Each SST range covers an interval of 0.5 K with its midpoint value given in the table, except for the first and last ranges. For the first range (labeled 301.25 K), all cloud objects with mean SSTs between 296.2 and 301.5 K are included, while all cloud objects with SSTs between 303 and 306 K are included for the last range (labeled 303.25 K).

A few characteristics of the frequencies of occurrence are apparent in Table 4. First, there are relatively small numbers of the S- and M-size cloud objects in the 303.25-K range. Second, more than half of the L-size cloud objects occurred in SSTs between 302 and 303 K (258 out of 476). Third, the number of the L-size cloud objects in the 303.25-K range is only slightly less than that of the 301.25-K range that covers very large mean SST variations. These results, in particular, the ratios of L size to all sizes shown in Table 4, indicate that higher SSTs, but not extremely high SSTs (303.25 K), are preferred by the L-size cloud objects during the 1998 El Niño period, which is consistent with the result shown by Lin et al. (2006) for the tropical cloud clusters defined with less stringent selection criteria than those used in the present study.

b. Statistical properties of cloud objects

Figure 4 shows a comparison of summary histograms for the L-size cloud objects among the five SST ranges. Clearly, the SST histograms are different among these SST ranges. Four of them have narrow distributions with SST variations being less than 2 K, while the 301.25-K range has a wide distribution of SST (mainly from 298 to 303 K). In the 301.25-K range, the high SST end of the distribution is composed of some cloud objects that are narrow and longitudinally oriented and some that are partially located over land, while the low SST end of the distribution is mostly due to other cloud objects with mean SSTs far less than 301 K.

Despite the large differences in the SST distributions, several parameters are similar from one SST range to another, including TOA albedo, IWP, τ, and ice particle size (Figs. 4c,f–h). This is confirmed by the statistical significance testing results shown in Table 5, which show the results between the consecutive SST ranges (columns 1–4), the second and fourth SST ranges (column 5), and the first and last SST ranges (column 6). A possible explanation for these observed features is that the L-size cloud objects are so optically thick (Fig. 2h) that their optical properties are not impacted by the underlying SSTs. Because of the insensitivity of τ to SST, other retrieved cloud microphysical properties and TOA albedo are also similar among the five SST ranges. Since the S-size cloud objects have smaller τ, the insensitivity does not hold well, as shown later.

Cloud macrophysical properties and OLR are rather different among the analyzed SST ranges (Figs. 4b,d,e) except for those between the 301.75- and 302.25-K

TABLE 5. The statistical significance levels or p values between a pair of SST ranges for different parameters of the large-size category of tropical convective cloud objects. Values below 0.05 are in bold and indicate statistically significant differences between two SST ranges, or at least 95% confidence that the two SST ranges are significantly different.

	Pairs of SST ranges					
Parameter	301.25 K, 301.75 K	301.75 K, 302.25 K	302.25 K, 302.75 K	302.75 K, 303.25 K	301.75 K, 302.75 K	301.25 K, 303.25 K
SST	**<0.001**	**<0.001**	**<0.001**	**<0.001**	**<0.001**	**<0.001**
OLR	0.129	0.853	**0.040**	**0.014**	**0.035**	**<0.001**
Albedo	0.142	0.766	0.252	0.263	0.455	0.159
Cloud height	**0.029**	0.788	**0.015**	**0.028**	**0.007**	**<0.001**
Cloud temperature	0.095	0.804	0.052	**0.020**	0.051	**<0.001**
Ice water path	0.420	0.807	0.235	0.208	0.278	0.564
Ice particle size	0.896	0.241	0.426	0.352	0.455	0.097
Optical depth	0.682	0.741	0.581	0.435	0.223	0.710

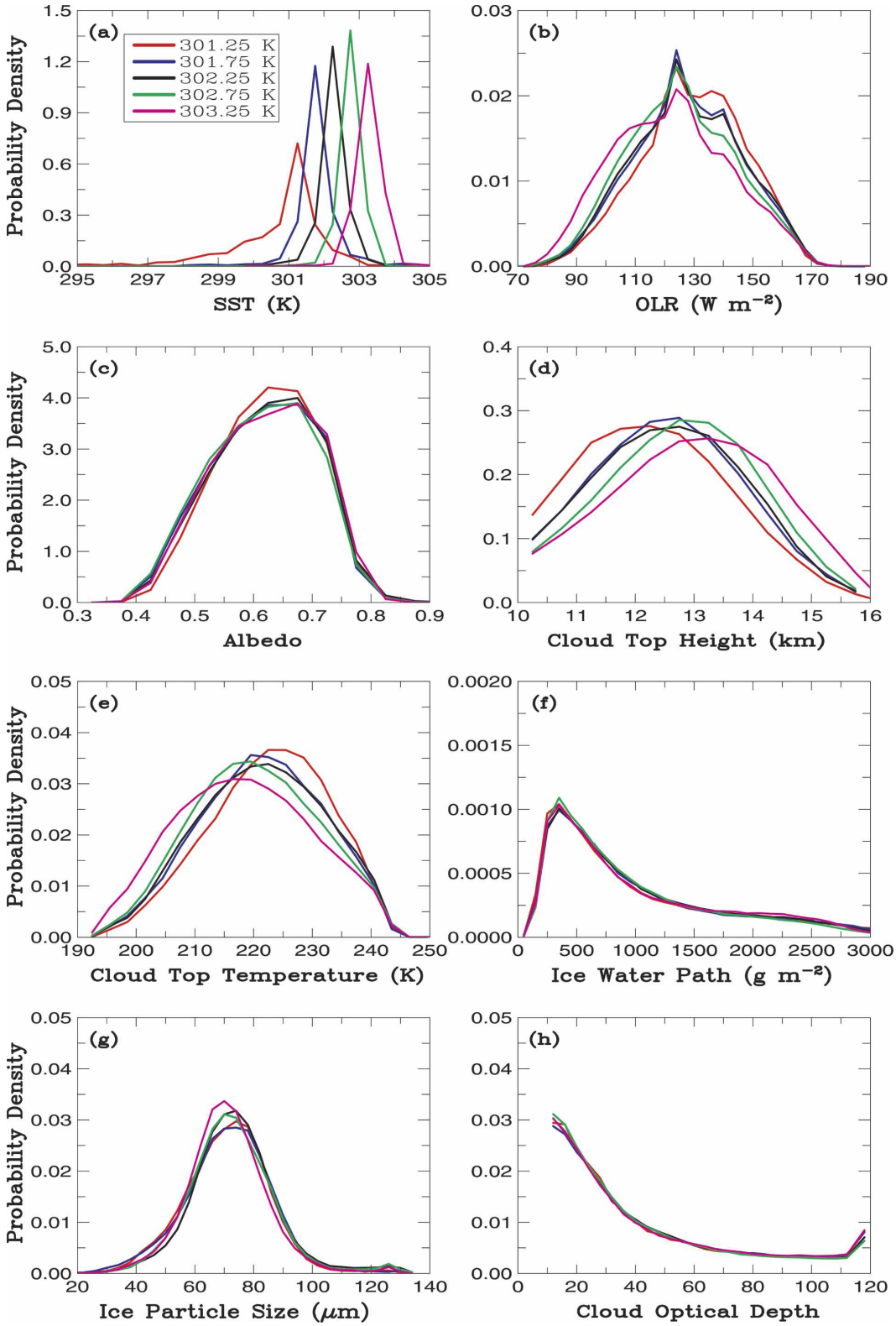

FIG. 4. Same as in Fig. 2 except for large-size category of cloud objects classified according to different SST ranges. Five SST ranges as labeled in the legend of (a) are shown in different colors.

TABLE 6. Same as in Table 5 except for the medium-size category of cloud objects.

Parameter	Pairs of SST ranges					
	301.25 K, 301.75 K	301.75 K, 302.25 K	302.25 K, 302.75 K	302.75 K, 303.25 K	301.75 K, 302.75 K	301.25 K, 303.25 K
SST	**<0.001**	**<0.001**	**<0.001**	**<0.001**	**<0.001**	**<0.001**
OLR	0.169	**0.019**	0.469	**0.039**	**0.012**	**<0.001**
Albedo	0.063	0.336	0.573	0.787	0.918	0.080
Cloud height	0.091	**0.002**	0.887	**0.041**	**<0.001**	**<0.001**
Cloud temperature	0.262	**0.013**	0.700	**0.041**	**0.010**	**<0.001**
Ice water path	0.608	0.484	0.175	0.395	0.146	**0.011**
Ice particle size	0.311	0.366	0.390	0.200	**0.039**	0.054
Optical depth	0.349	0.134	0.688	0.067	0.215	**0.002**

ranges (Table 5). For the lower SST ranges, OLR and cloud temperature tend to be more negatively skewed while cloud height tends to be more positively skewed. The differences in the modes of the distributions of cloud height and temperature between the 301.25 and 303.25-K ranges are as great as or greater than those between the S- and L-size categories of cloud objects discussed earlier (Fig. 2). In OLR, the mode at 140 W m^{-2} is more pronounced for the lower SST ranges. This result can, as shown later, be related to weaker large-scale ascents of cloud objects in the lower SST ranges, resulting in relatively shallower convective systems.

Besides the differences discussed in section 3b, the M-size category has slightly different and sometimes stronger dependency of their properties on the SST ranges (Figs. 5a,c,e,g) compared to the L-size category. First, cloud microphysical and optical properties show slightly more significant differences among some of the SST ranges (Table 6), for example, between the 301.25- and 303.25-K ranges. Second, similar distributions of cloud macrophysical properties and OLR are found between the 301.25- and 301.75-K ranges and between the 302.25- and 302.75-K ranges (Figs. 5c,e,g), instead of between the 301.75- and 302.25-K ranges as found in the L-size category (Figs. 4b,d,e).

The S-size category of cloud objects shows more differences from the M-size category of cloud objects (Figs. 5b,d,f,h and Table 7) in terms of how the cloud properties change with SSTs. First, TOA albedo, IWP, and τ show small differences among the analyzed SST ranges (Table 7) although the distributions of ice particle sizes show significant differences among some SST ranges. Second, all cloud properties are rather similar among the three highest SST ranges and between the two lowest SST ranges (Table 7). Their distributions for the two lowest SST ranges are, however, different from those of the three highest SST ranges (Figs. 5d,f,h). The distributions of the lowest two SST ranges have pronounced peaks in OLR between 140 and 150 W m^{-2} while the peak at 124 W m^{-2} becomes secondary. The latter peak is associated with strong convective systems. These results suggest that many of the S-size cloud objects in the three highest SST ranges may be associated with strong convective systems that are split by satellite swaths and/or developing convective systems that had not yet reached the L-size category, as far as their macrophysical properties are concerned (cf. Figs. 5d,f,h with Figs. 2b,d,e).

c. Linkage with large-scale dynamics

The ω frequency departures from Fig. 3a are plotted in Fig. 6 for all five SST ranges of the L-size category. The magnitude of the departures exceeding 0.6% appears very often, with some exceeding 1.0%, which is

TABLE 7. Same as in Table 5 except for the small-size category of cloud objects.

Parameter	Pair of SST ranges					
	301.25 K, 301.75 K	301.75 K, 302.25 K	302.25 K, 302.75 K	302.75 K, 303.25 K	301.75 K, 302.75 K	301.25 K, 303.25 K
SST	**<0.001**	**<0.001**	**<0.001**	**<0.001**	**<0.001**	**<0.001**
OLR	0.434	**0.003**	0.266	0.760	**<0.001**	**<0.001**
Albedo	0.454	0.875	0.934	0.632	0.948	0.711
Cloud height	0.094	**<0.001**	0.240	0.856	**<0.001**	**<0.001**
Cloud temperature	0.631	**0.002**	0.393	0.924	**<0.001**	**<0.001**
Ice water path	0.463	0.294	0.896	0.617	0.202	0.332
Ice particle size	0.056	**0.016**	0.875	0.981	**0.022**	0.191
Optical depth	0.731	0.734	0.918	0.771	0.909	0.622

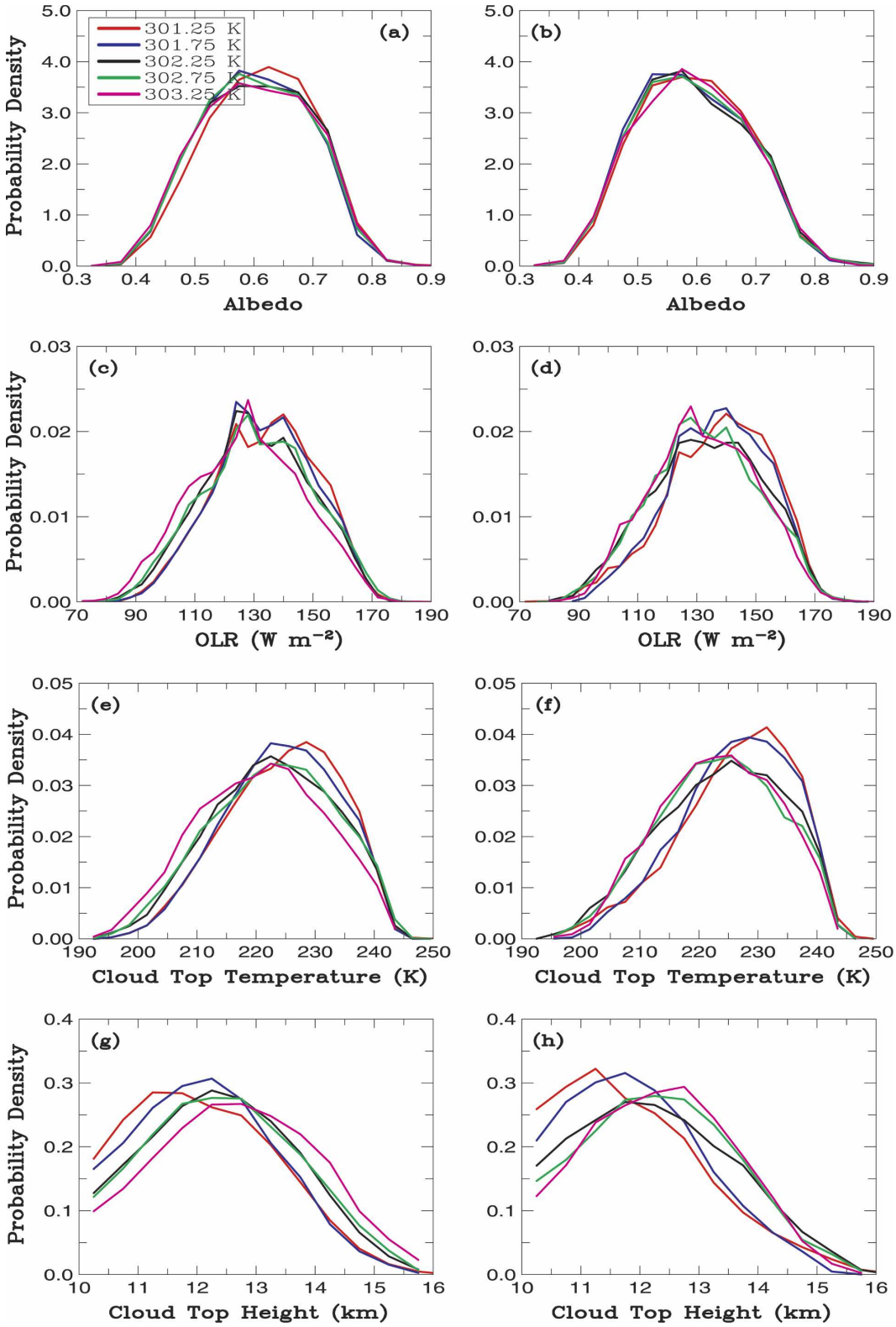

FIG. 5. Same as in Fig. 4 except for the (a), (c), (e), (g) medium- and (b), (d), (f), (h) small-size cloud objects classified according to SST ranges. Only histograms of (a), (b) TOA albedo, (c), (d) OLR, (e), (f) cloud temperature, and (g), (h) height are shown. Five SST ranges as labeled in the legend of (a) are shown in different colors.

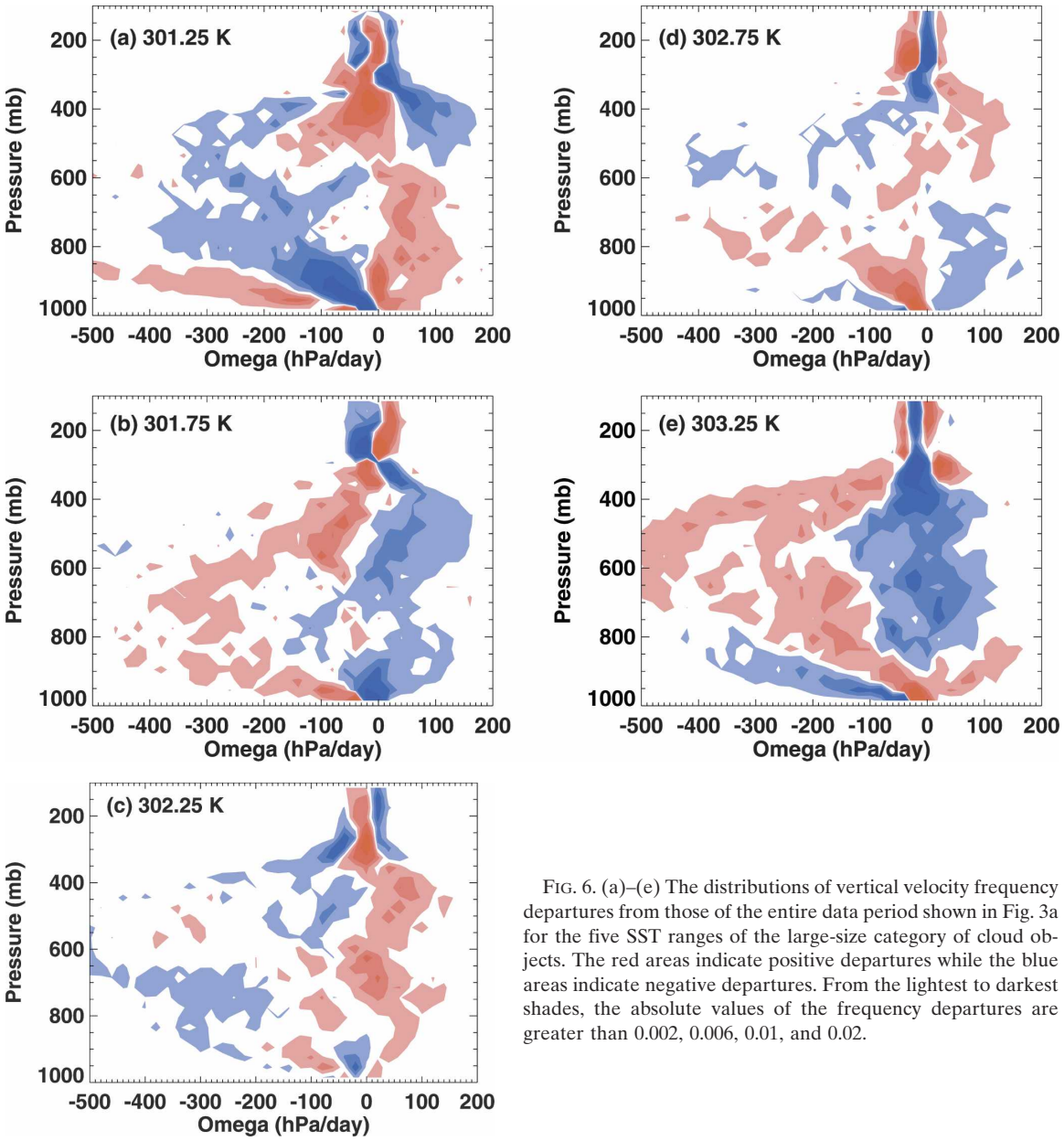

FIG. 6. (a)–(e) The distributions of vertical velocity frequency departures from those of the entire data period shown in Fig. 3a for the five SST ranges of the large-size category of cloud objects. The red areas indicate positive departures while the blue areas indicate negative departures. From the lightest to darkest shades, the absolute values of the frequency departures are greater than 0.002, 0.006, 0.01, and 0.02.

the lowest shaded value plotted in Fig. 3a. Two distinct features can be pointed out from Fig. 6. First, more frequent occurrences of upward motion ($\omega < -50$ hPa day^{-1}) are seen in the lowest 150 hPa in the lowest SST range, while the opposite is true for the highest SST range. This means that stronger low-level upward motion, which acts as a trigger, is required to produce large convective systems when the SST is lower. Second, the differences in cloud macrophysical properties shown in Fig. 4 cannot be explained by those in the vertical velocity frequency alone. For example, the 301.75- and 302.25-K ranges show no significant difference in cloud macrophysical properties, but there are more frequent occurrences of upward motions in the 301.75-K range. Therefore, the higher SST in the 302.25-K range has to compensate for the weaker ascent motions. Another example to support this point is the overall similarity in the ω frequency distributions between the 302.25- and 302.75-K ranges, but the cloud macrophysical properties are different between these two SST ranges (Table 5).

The ω_{500} frequency distributions for the five SST ranges are shown in Fig. 7 for all three size categories. Two features appearing in Fig. 7 are worth pointing out. First, the differences in the ω_{500} distribution are greater between some pairs of SST ranges for the S- and M-size categories, compared to the L-size category. For ex-

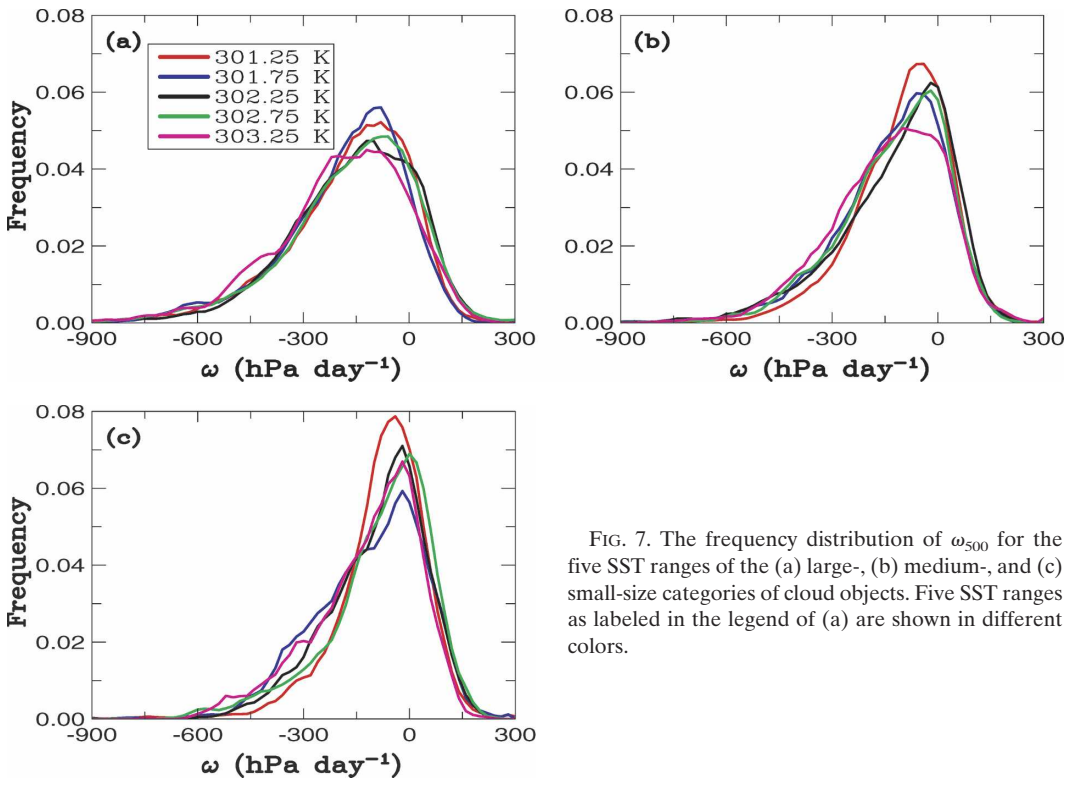

FIG. 7. The frequency distribution of ω_{500} for the five SST ranges of the (a) large-, (b) medium-, and (c) small-size categories of cloud objects. Five SST ranges as labeled in the legend of (a) are shown in different colors.

ample, the frequencies corresponding to the modes of the 301.25- and 303.25-K distributions differ by ~2% for both the S- and M-size categories. These large differences in the ω_{500} distribution between two SST ranges can be related to the large differences seen in the cloud macrophysical properties of the S- and M-size categories (Fig. 5). Second, the large differences among pairs of SST ranges occur mainly over the negative ω_{500} side of the diagrams, suggesting that the SST differences can impact the ascending regions of the matched ECMWF rectangles, that is, cloud objects themselves. These results suggest that impact of SST on the large-scale dynamics seems to be stronger for the smaller-size categories of cloud objects. The combination of SST with large-scale dynamics may explain the larger differences in the statistical properties between some pairs of the five SST ranges shown in Figs. 4 and 5.

5. Variations of cloud object characteristics with satellite precession cycle

a. Frequency of occurrence

Table 8 shows the number of cloud objects in the Pacific that are classified according to satellite precession cycles. The numbers of cloud objects are obtained for five precession cycles of each of the three size categories. The TRMM precession cycle is 46 days long. The first precession cycle was selected to begin on 14 January 1998 (ending on 28 February) instead of 1 January 1998 for the sake of labeling these cycles and is labeled "Jan–Feb" cycle. The other precession cycles are labeled Mar–Apr (1 March–15 April), Apr–May (16 April–31 May), Jun–Jul (1 June–16 July), and Jul–Aug (17 July–31 August), respectively.

It appears that the total number of all-size cloud objects in each precession cycle is roughly the same, that is, within 20% of each other (Table 8). The differences in the number of cloud objects among the precession cycles are larger for individual size categories. The number of cloud objects in the S-size category is the largest in the Jul–Aug cycle and the smallest in the Jan–Feb cycle. The M-size cloud objects also have the largest number of occurrences in the Jul–Aug cycle. This result is related to low SSTs in the Jul–Aug cycle. The L-size category has a higher number of cloud objects in the Jan–Feb cycle, corresponding to the peak phase of the 1997/98 El Niño.

b. Statistical properties of cloud objects

Figure 8a shows the SST distributions of the L-size category for the five precession cycles. From January to August 1998, the probability densities for SSTs greater than 302 K decrease as the El Niño dissipates. This is indicated by the shift in distribution toward lower SSTs

TABLE 8. Number of observed cloud objects during the five precession cycles for three cloud object size categories. The cloud object size is in terms of its equivalent diameter. The ratios of large size to all sizes are also shown for the number of cloud objects [ratio (number)] and the total number of footprints [ratio (footprint)].

Size category	Jan–Feb	Mar–Apr	Apr–May	Jun–Jul	Jul–Aug
Small	133	158	137	151	173
Medium	157	178	143	142	190
Large	121	83	82	82	91
Total	411	419	362	375	454
Ratio (number)	0.294	0.201	0.227	0.219	0.200
Ratio (footprint)	0.738	0.617	0.692	0.625	0.593

with the progress of precession cycles. The SST distribution is approximately normally distributed in the Jul–Aug cycle. In the other four cycles, the SST pdfs are skewed toward higher SSTs. The statistical significance tests show that the SST distributions between most pairs of the precession cycles are statistically different (Table 9), especially those of nonconsecutive cycles. The exceptions are between the first two precession cycles during the peak period of the El Niño and between the Apr–May and Jun–Jul cycles.

Visual inspection of the rest of the panels in Fig. 8 shows that the spread of the five precession-cycle distributions is not as great as that seen from Fig. 4 among the five SST-range distributions for cloud macrophysical properties, but slightly greater for cloud microphysical and optical properties and TOA albedo. These are important distinctions between these two sets of results because differences in the collective large-scale dynamics (for an ensemble of cloud objects) among the precession cycles tend to be smaller than those among the SST ranges. This is because an ensemble of cloud objects are sampled from every tropical Pacific region within a given precession cycle instead of those subregions that lie within an SST range for a long period.

The most important parameter for validating the FAT hypothesis of Hartmann and Larson (2002), as discussed in the introduction, is the cloud-top temperature. All pdfs of cloud-top temperature are nearly normally distributed except for being slightly skewed toward the high values of cloud-top temperature (Fig. 8e). The most striking feature shown in Fig. 8e is that most of the pdfs are not statistically different from each other despite the statistically significant differences in the SST distributions among some precession cycles (Table 9). The exceptions are the moderate differences between the Mar–Apr and Apr–May cycles and between the Jan–Feb and Jul–Aug cycles, with p values being between 0.05 and 0.10. These differences among some pairs of precession cycles appear mainly in the high temperature ranges (>215 K) but not in the low temperature ranges. For the purpose of comparison, this statement is not true for the different SST ranges (Fig. 4e) shown in section 4b. The similarity in the low temperature ranges of pdfs among the precession cycles, therefore, suggests that there is strong evidence for supporting the FAT hypothesis of Hartmann and Larson (2002).

Cloud height is another cloud macrophysical property that shows no statistically significant differences among the precession cycles except for between the first and last precession cycles and so does the OLR (Table 9). This result can be visually confirmed from Figs. 8b,d. Cloud-top height is obviously related to the strength of large-scale dynamics because stronger large-

TABLE 9. The statistical significance levels or p values between a pair of precession cycles for different parameters of the large-size categories of cloud objects. Values below 0.05 are in bold and indicate statistically significant differences between two precession cycles, or at least 95% confidence that the two precession cycles are significantly different.

	Pairs of precession cycles					
Parameter	Jan–Feb, Mar–Apr	Mar–Apr, Apr–May	Apr–May, Jun–Jul	Jun–Jul, Jul–Aug	Mar–Apr, Jun–Jul	Jan–Feb, Jul–Aug
SST	0.602	**0.033**	0.257	**0.004**	**0.004**	**<0.001**
OLR	0.132	0.125	0.119	0.426	0.172	**0.046**
Albedo	0.806	**0.023**	0.587	0.842	0.057	0.103
Cloud height	0.686	0.150	0.522	0.356	0.127	**0.005**
Cloud temperature	0.774	0.095	0.178	0.552	0.231	0.084
Ice water path	0.608	0.074	0.166	0.494	**0.049**	**0.021**
Ice particle size	0.452	**0.035**	**0.026**	0.118	0.057	**0.035**
Optical depth	0.581	**0.024**	0.670	0.787	**0.004**	**0.028**

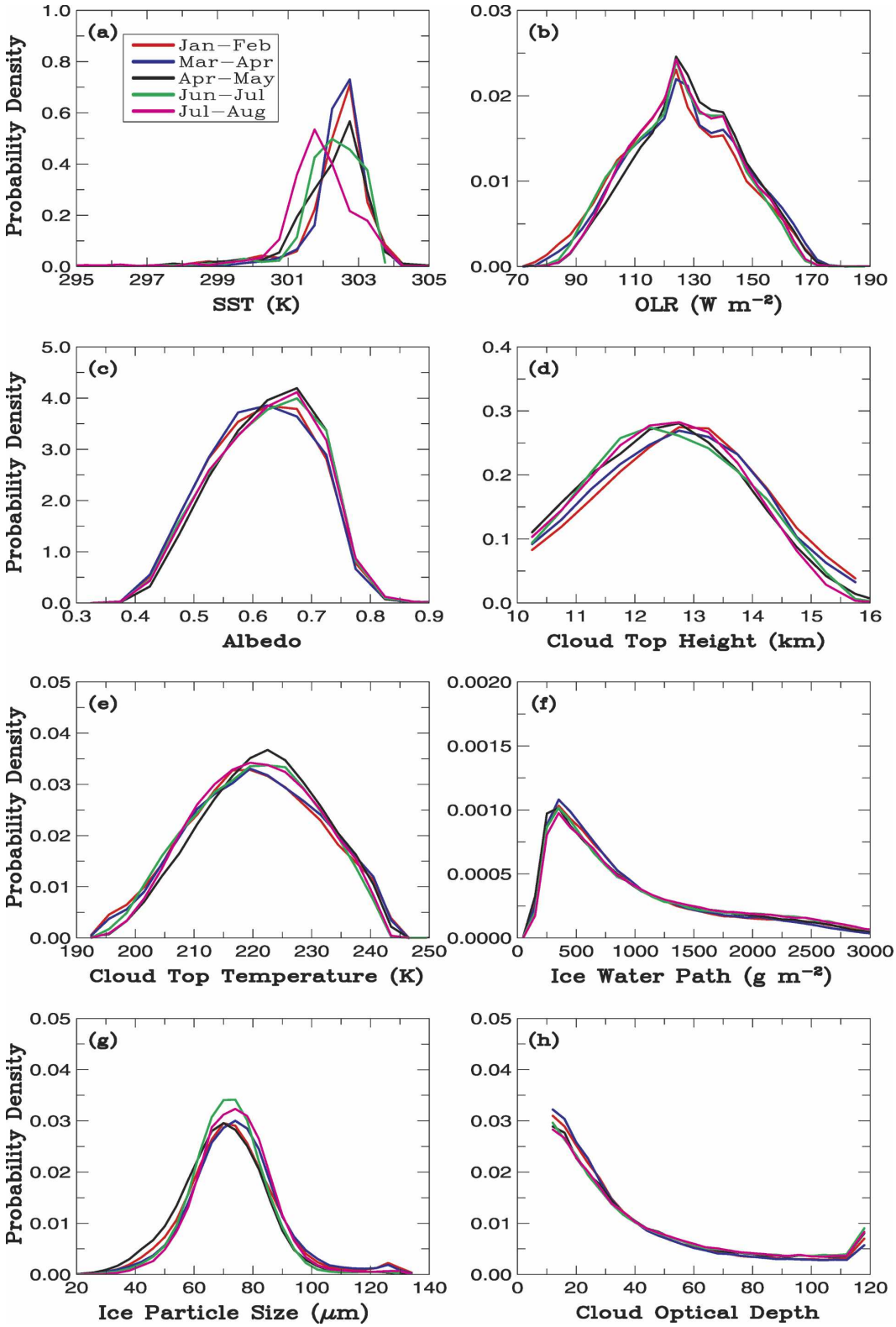

FIG. 8. Same as in Fig. 2 except for the large-size category of cloud objects classified according to satellite precession cycles. Five precession cycles as labeled in the legend of (a) are shown in different colors.

TABLE 10. Same as in Table 9 except for the medium-size categories of cloud objects.

Parameter	Pairs of precession cycles					
	Jan–Feb, Mar–Apr	Mar–Apr, Apr–May	Apr–May, Jun–Jul	Jun–Jul, Jul–Aug	Mar–Apr, Jun–Jul	Jan–Feb, Jul–Aug
SST	0.166	0.568	**0.005**	**0.048**	**<0.001**	**<0.001**
OLR	0.125	**0.003**	**0.002**	0.567	0.211	0.138
Albedo	0.227	0.509	0.072	0.446	0.291	0.111
Cloud height	0.068	**<0.001**	0.358	0.663	**0.039**	0.394
Cloud temperature	**0.024**	**0.001**	**0.008**	0.650	0.199	**0.029**
Ice water path	0.395	0.196	0.142	0.092	0.138	**0.028**
Ice particle size	0.303	**0.030**	0.198	**0.019**	**<0.001**	0.707
Optical depth	0.504	0.828	0.069	0.406	**0.027**	0.078

scale ascent can increase the overall cloud height of convective systems, which can skew the cloud-height distribution toward higher values. The lack of statistically significant differences in cloud height among the precession cycles is additional evidence for further supporting the FAT hypothesis. As discussed in Part I, cloud-top height can be different if the stratification of the atmosphere changes significantly, for example, between the Jan–Feb (the peak phase of El Niño) and Jul–Aug (the dissipative phase of El Niño) cycles.

The findings discussed above do not include the contributions of optically thin ($\tau < 10$) upper-tropospheric clouds. These clouds are a major contributor to the tropical cloud population and radiative budget, but a majority of them are tied to the optically thick clouds examined in this study. They will be studied to validate the FAT hypothesis in the future.

The statistically significant differences in cloud microphysical properties, TOA albedo, and τ among some precession cycles for the L-size category are related to the distributions in one or two particular precession cycles that are very different from other precession cycles (Fig. 9 and Table 9), for example, the Mar–Apr cycle. No systematic difference is present in their distributions shown in Fig. 8.

For the S- and M-size cloud objects, the differences in SST distribution between two precession cycles are not necessarily larger than those of the L-size cloud objects (Tables 9–11). The last two precession cycles show significant differences in the SST distributions from the earlier cycles and between each other. However, these differences do not translate into statistically significant differences in cloud macrophysical and microphysical properties. As with cloud microphysical and optical properties of the L-size category, one or two particular precession cycles show the most pronounced differences from the other precession cycles. For cloud height, temperature, and OLR, significantly different distributions are found for the Mar–Apr cycle of the M-size category and the Jun–Jul cycle of the S-size category (Fig. 9), suggesting that the FAT hypothesis is less well supported for these size categories. Most of the cloud microphysical properties and TOA albedo, however, are not significantly different from other precession cycles for these particular precession cycles of the S- and M-size categories. This result is similar to that found in the different SST ranges discussed in section 4b. This similarity suggests that the collective large-scale dynamics may be less similar among precession cycles for the S- and M-size categories compared to that

TABLE 11. Same as in Table 9 except for the small-size category of cloud objects.

Parameter	Pairs of precession cycles					
	Jan–Feb, Mar–Apr	Mar–Apr, Apr–May	Apr–May, Jun–Jul	Jun–Jul, Jul–Aug	Mar–Apr, Jun–Jul	Jan–Feb, Jul–Aug
SST	0.184	0.461	0.267	**0.013**	**0.022**	**<0.001**
OLR	0.254	0.503	0.216	**0.012**	**0.012**	0.202
Albedo	0.573	0.774	0.502	0.303	0.404	**0.019**
Cloud height	0.690	0.372	0.249	**0.025**	**0.008**	0.088
Cloud temperature	0.766	0.362	0.200	**0.007**	**0.008**	0.139
Ice water path	**0.017**	0.205	0.561	0.134	0.385	**0.003**
Ice particle size	**0.004**	**0.028**	0.378	0.287	**0.005**	0.211
Optical depth	0.504	0.796	0.274	0.241	0.094	**0.003**

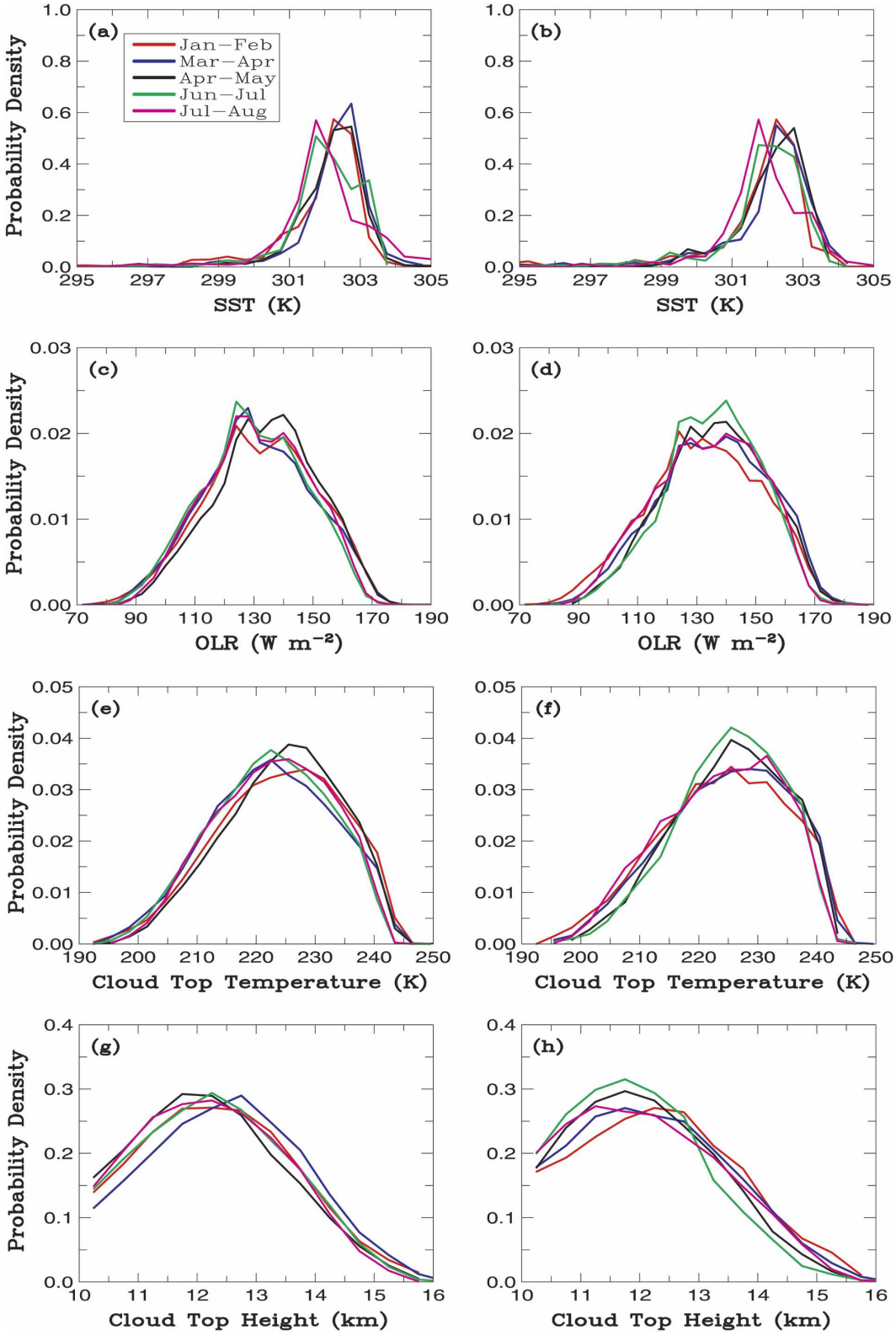

FIG. 9. Same as in Fig. 2 except for the (a), (c), (e), (g) medium- and (b), (d), (f), (h) small-size categories of cloud objects classified according to satellite precession cycles. Only histograms of (a), (b) TOA albedo, (c), (d) OLR, (e), (f) cloud temperature, and (g), (h) height are shown. Five precession cycles as labeled in the legend of (a) are shown in different colors.

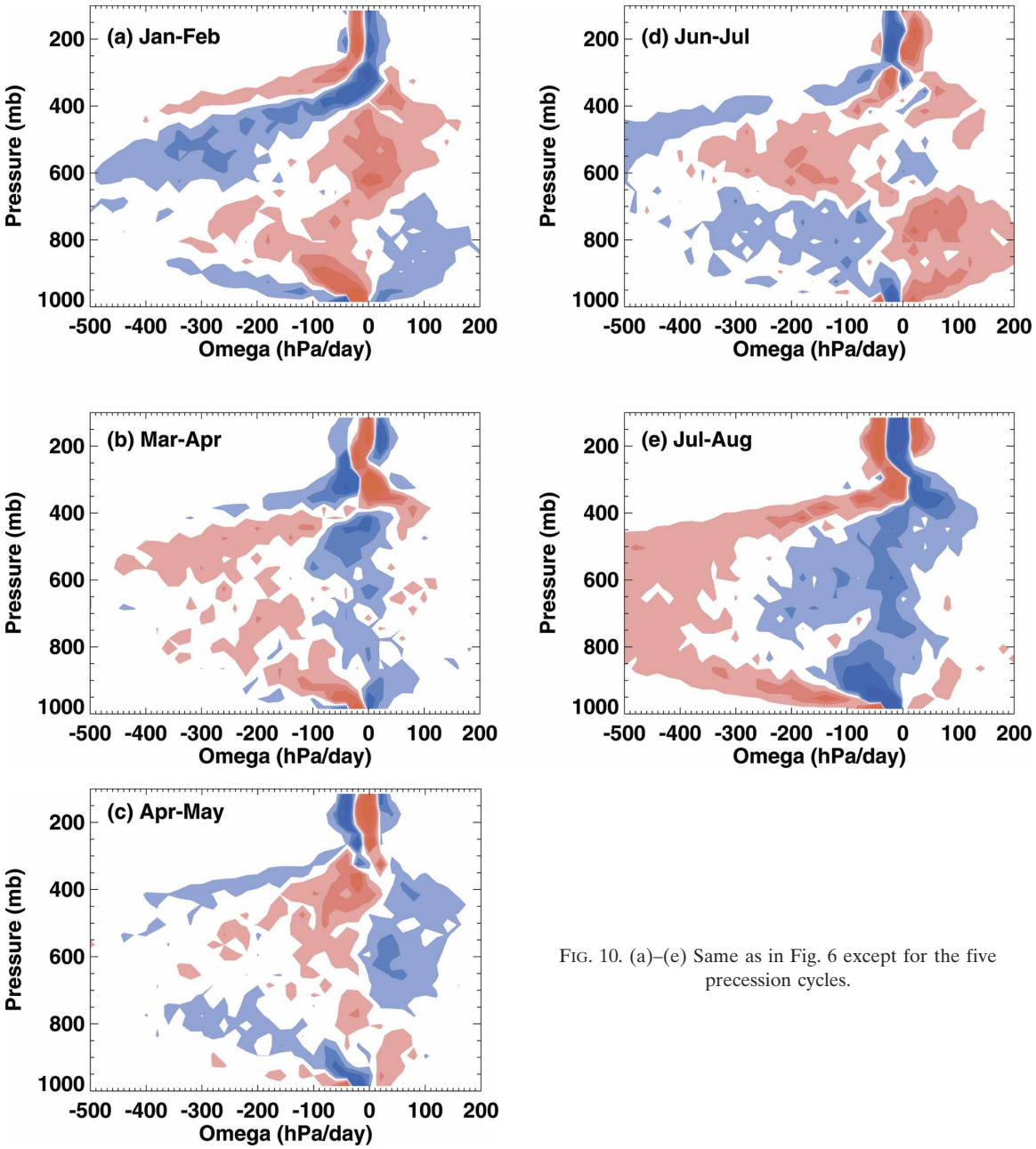

FIG. 10. (a)–(e) Same as in Fig. 6 except for the five precession cycles.

of the L-size category. This is probably the main reason why there is less evidence for supporting the FAT hypothesis for the S- and M-size categories.

c. Linkage with large-scale dynamics

The ω frequency departures from Fig. 3a are plotted in Fig. 10 for all five precession cycles of the L-size category. The magnitudes of the departures are mostly between -0.2% and $+0.2\%$, with small areas over 1.0%. The small differences in both the large-scale dynamics and SST among the precession cycles contribute to small differences in cloud macrophysical properties, compared to those among the SST ranges discussed in section 3b. There are, however, some differences in the ω frequency diagrams among the five precession cycles. For example, the frequency distributions of the Jul–Aug cycle (low SST) at all heights are more skewed toward higher magnitudes of upward motion compared to those of the Jan–Feb cycle. The stronger vertical motions, particularly those below 850 hPa, compensate for the lower SSTs of the Jul–Aug cycle.

The differences among the five precession cycles are

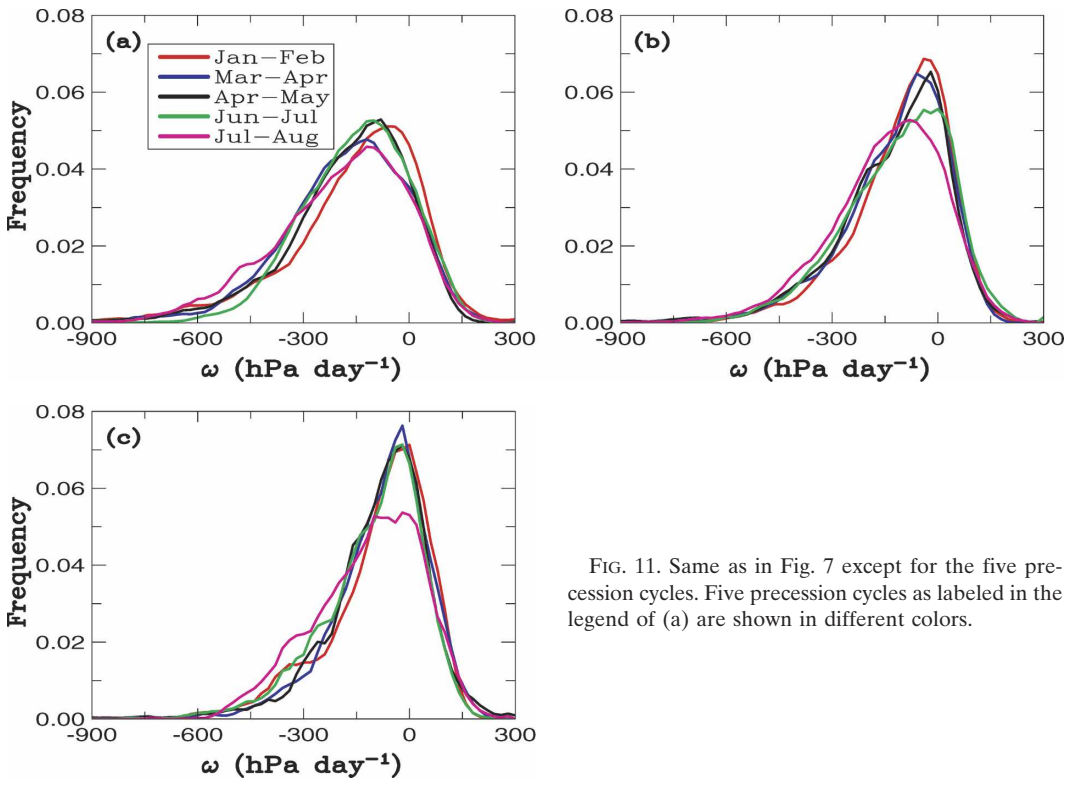

FIG. 11. Same as in Fig. 7 except for the five precession cycles. Five precession cycles as labeled in the legend of (a) are shown in different colors.

generally larger for the S- and M-size categories than for the L-size category. This can be seen from the frequency distributions of ω_{500} for the five precession cycles (Fig. 11) of all three size categories. For example, the frequency difference corresponding to the modes of ω_{500} between the Jan–Feb and Jul–Aug cycles of the S-size category is about 3%. It is about half as large for the M-size category but less than 0.5% for the L-size category. This result suggests that large-scale dynamics are more likely to be different for the smaller-size categories of cloud objects. Consequently, the differences in cloud macrophysical properties are larger for the S- and M-size cloud objects among some precession cycles compared to the L-size cloud objects (Fig. 9). But these differences in large-scale dynamics are not as large as those among the different SST ranges (Fig. 7) or among the different size categories (Fig. 3).

6. Conclusions and discussion

In this study, characteristics of tropical convective cloud objects observed over the tropical Pacific during January–August 1998 have been examined using the TRMM/CERES data, emphasizing evidence for supporting the fixed anvil temperature (FAT) hypothesis of Hartmann and Larson (2002). These characteristics include the frequencies of occurrence and statistical distributions of cloud microphysical, macrophysical, optical, and radiative properties. Their variations with cloud object size, SST, and satellite precession cycle have been analyzed, as well as the corresponding frequency distributions of the cloud object matched vertical velocity.

It is found that statistical distributions of cloud physical properties are significantly different among three size categories of cloud objects with equivalent diameters of 100–150, 150–300, and >300 km, except for those of ice particle size. The distributions for the larger-size category of cloud objects are more skewed toward high SSTs, high cloud tops, low cloud-top temperature, large ice water path, high τ, low outgoing LW radiation, and high TOA albedo than the smaller-size category. Physical interpretations for these differences are that the larger cloud objects are associated with stronger convective systems so that both cumulonimbi and thick anvils penetrate closer to the tropopause. The weaker convective systems or loosely organized cloud clusters, on the other hand, are broken into several small cloud objects because the cloud objects are required to be contiguous by definition. Very few small-size cloud objects result from truncation by narrow satellite swaths from the strong convective systems. The frequency distributions of the matched vertical velocity confirm that there are significant differences in the

large-scale dynamics among the three size categories of cloud objects. These distributions of vertical velocity are more negatively skewed for larger-size cloud objects that favor the existence of stronger convective systems.

As SST varied from one satellite precession cycle to another, the changes in macrophysical properties of cloud objects over the entire tropical Pacific were small for the large-size category of cloud objects, relative to those of the small- and medium-size categories. This evidence supports the FAT hypothesis for the large-size category. Combined with the result that a higher percentage of the large-size category of cloud objects occurs during higher SST subperiods, this implies that macrophysical properties of cloud objects would be less sensitive to further warming of the climate if the collective large-scale dynamics remain relatively unchanged. This conclusion is tentative because optically thin ($\tau < 10$) upper-tropospheric clouds are not included and uncertainties associated with remotely sensed data products are not fully incorporated in the present analysis. In addition, the data period is relatively short. Long-period data from the *Terra* satellite will be used in a future study.

It is also found that some cloud microphysical properties, TOA albedo and τ, are significantly different between some precession cycles for the large-size category even though cloud macrophysical properties are not. This characteristic is found in the small- and medium-size cloud objects for some pairs of precession cycles. The frequency distributions of the matched large-scale vertical velocity show small differences among the precession cycles for the large-size category, relative to those for the small- and medium-size categories. This is consistent with the observation that statistical distributions of cloud macrophysical properties are not significantly different among the precession cycles for the large-size category.

On the other hand, the large-scale dynamics play more important roles in determining the statistical characteristics of cloud objects when they are classified as a function of SST or size category instead of as a function of satellite precession cycle. This is the major reason why the FAT hypothesis is less well supported by the results from the former two classifications. Specifically, statistical characteristics of cloud microphysical properties, optical depth, and TOA albedo are not sensitive to the SST, but those of cloud macrophysical properties including cloud-top temperature are dependent upon the SST. This feature is also present in some of the five precession cycles of the small- and medium-size categories of cloud objects. This is due to the fact that large-scale dynamics are less similar for these precession cycles of the small- and medium-size categories of cloud objects.

Further studies will be performed to compare statistical properties from observations and high-resolution cloud model simulations to validate the FAT hypothesis. Results from simulations of the tropical convective cloud objects observed in March 1998 show that a 2D cloud-resolving model can do a better job in capturing the differences in cloud microphysical properties among three size categories than those for the cloud macrophysical properties (Luo et al. 2007). This result may suggest that it might be difficult to validate the FAT hypothesis with 2D simulations, although 3D simulations in a radiative–convective equilibrium setting supports the FAT hypothesis (Kuang and Hartmann 2007). Further study will be needed to investigate the ability of 3D models in capturing these observed differences.

Acknowledgments. The CERES data were obtained from the Atmospheric Sciences Data Center at the NASA Langley Research Center. This research has been supported by NASA EOS interdisciplinary study program (Dr. D. Anderson) and by the NSF Grant ATM-0336762. The authors would also like to acknowledge Dr. Bruce Barkstrom of Langley Research Center and Professor David Randall of Colorado State University for their earlier insightful vision to this project and Dr. Patrick Minnis for providing the uncertainty estimates. We thank two anonymous reviewers for their constructive comments.

APPENDIX

Effect of Uncertainties

This appendix provides an assessment of the impact of uncertainties in measured parameters on the summary histograms of these parameters discussed in this paper. It is challenging to assign rigorous uncertainty

TABLE A1. The systematic biases and random errors in the measured footprint data and bin intervals of histograms used in this study.

Parameter	Systematic bias	Random error	Bin interval of histogram
OLR (W m^{-2})	—	4.3	4
TOA SW (W m^{-2})	—	12.9	20
Cloud height (km)	−0.5	0.8	0.5
Cloud temperature (K)	+3.5	5.5	3
Ice water path (g m^{-2})	<30%	40%	100
Ice particle size (μm)	<10%	20%	4
Optical depth	<20%	20%	4

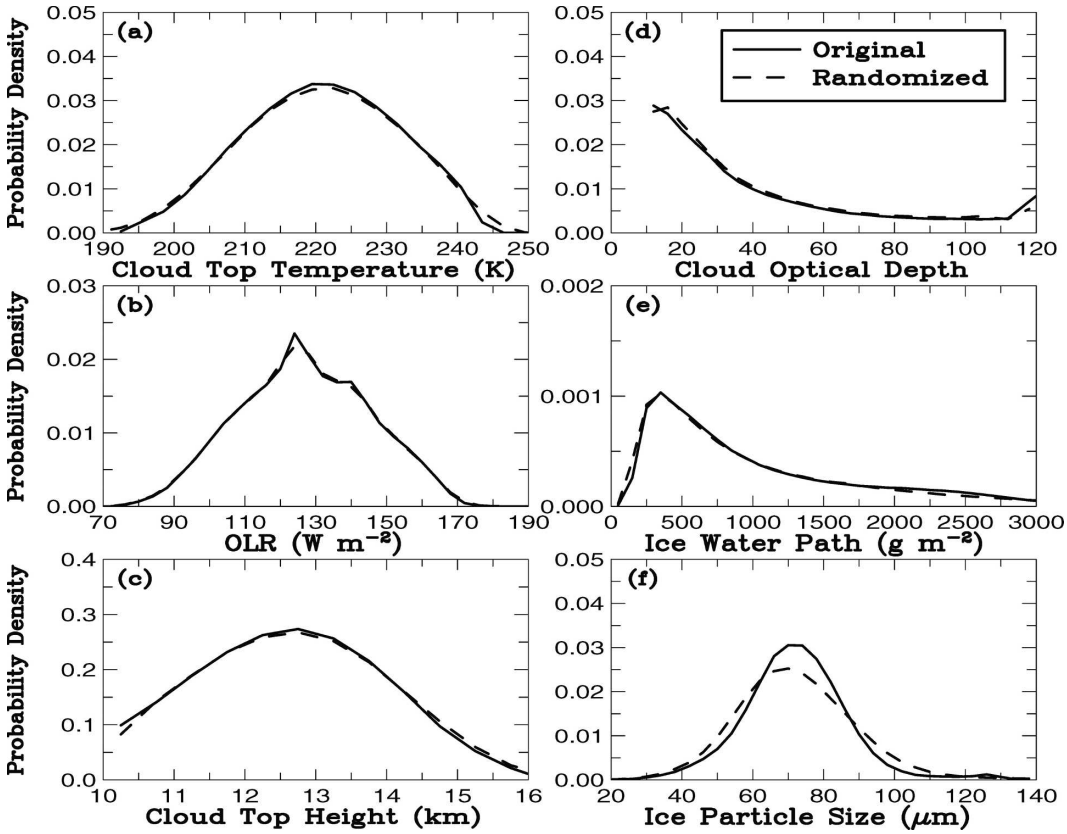

FIG. A1. Comparison of the original (same as the long-dashed curve in Fig. 2) and randomized summary histograms of (a) cloud-top temperature, (b) OLR, (c) cloud-top height, (d) cloud optical depth, (e) ice water path, and (f) ice diameter for the large-size category of cloud objects.

estimates to remotely sensed products, especially for those parameters such as the top-of-the-atmosphere SW and LW radiative fluxes that lack direct validation measurements (Wielicki et al. 1995). The strategy is to add random noise to the footprint data and then reproduce the histograms for all parameters discussed in this paper. The systematic biases and random errors are listed in Table A1, along with the bin intervals used for generating the histograms. The uncertainty values are provided by Wielicki et al. (1995) for SW and LW radiative fluxes. Uncertainties for retrieval of CERES ice cloud properties derived using the Moderate Resolution Imaging Spectroradiometer (MODIS) are taken from a combination of tests of different assumed ice crystal scattering phase functions (Mishchenko et al. 1996; Chepfer et al. 2002) and validation from satellite overpasses of the U.S. Department of Energy (DOE) Atmospheric Radiation Measurement (ARM) validation sites (Mace et al. 2005). While Mace et al. (2005) considered the more difficult case of ice clouds with optical depths less than 3, recent results for ice cloud with optical depths greater than 10 (used in the current study) showed similar uncertainties (J. Mace 2006, personal communication).

The summary diagrams of the randomized footprint data are compared with those shown in Fig. 2 for the large-size cloud objects only. Six parameters with the largest differences between these two sets of histograms are shown in Fig. A1. These differences except for those of ice diameter are much smaller than those among the size categories, mean SST ranges, and satellite precession cycles discussed earlier in the paper, partially because the random errors are not much larger than the bin intervals used in generating the histograms (Table A1). On the other hand, the systematic biases only shift the ranges of summary histograms slightly, which does not impact the conclusion. Therefore, the findings presented in this study are not likely to be impacted by both the random and systematic uncertainties.

REFERENCES

Barkstrom, B., E. F. Harrison, G. L. Smith, R. N. Green, J. Kibler, R. Cess, and the ERBE Science Team, 1989: Earth Radiation

Budget Experiment (ERBE) archival and April 1985 results. *Bull. Amer. Meteor. Soc.,* **70,** 591–598.

Bony, S., J.-L. Dufresne, H. Le Treut, J.-J. Morcrette, and C. Senior, 2004: On dynamic and thermodynamic components of cloud changes. *Climate Dyn.,* **22,** 71–86.

Cess, R. D., M. Zhang, P.-H. Wang, and B. A. Wielicki, 2001: Cloud structure anomalies over the tropical Pacific during the 1997/98 El Niño. *Geophys. Res. Lett.,* **28,** 4547–4550.

Chepfer, H., P. Minnis, D. Young, L. Nguyen, and R. F. Arduini, 2002: Estimation of cirrus cloud effective crystal shapes using visible reflectances from dual-satellite measurements. *J. Geophys. Res.,* **107,** 4730, doi:10.1029/2000JD000240.

Efron, B., and R. Tibshirani, 1993: *An Introduction to the Bootstrap.* Chapman and Hall, 456 pp.

Eitzen, Z. A., and K.-M. Xu, 2005: A statistical comparison of deep convective cloud objects observed by an Earth Observing System satellite and simulated by a cloud-resolving model. *J. Geophys. Res.,* **110,** D15S14, doi:10.1029/2004JD005086.

Fu, Q., M. Baker, and D. L. Hartmann, 2002: Tropical cirrus and water vapor: An effective earth infrared iris? *Atmos. Chem. Phys.,* **2,** 31–37.

Geng, Q., and M. Sugi, 2001: Variability of the North Atlantic cyclone activity in winter analyzed from NCEP–NCAR reanalysis data. *J. Climate,* **14,** 3863–3873.

Gray, W. M., and R. W. Jacobson Jr., 1977: Diurnal variation of deep cumulus convection. *Mon. Wea. Rev.,* **105,** 1171–1188.

Hartmann, D. L., and M. L. Michelsen, 1993: Large-scale effects on regulation of tropical sea surface temperature. *J. Climate,* **6,** 2049–2062.

——, and K. Larson, 2002: An important constraint on tropical cloud–climate feedback. *Geophys. Res. Lett.,* **29,** 1951, doi:10.1029/2002GL015835.

——, and M. L. Michelsen, 2002: No evidence for iris. *Bull. Amer. Meteor. Soc.,* **83,** 249–254.

Kuang, Z., and D. L. Hartmann, 2007: Testing the fixed anvil temperature hypothesis in a cloud-resolving model. *J. Climate,* in press.

Larson, K., and D. L. Hartmann, 2003a: Interactions among cloud, water vapor, radiation, and large-scale circulation in the tropical climate. Part I: Sensitivity to uniform sea surface temperature changes. *J. Climate,* **16,** 1425–1440.

——, and ——, 2003b: Interactions among cloud, water vapor, radiation, and large-scale circulation in the tropical climate. Part II: Sensitivity to spatial gradients of sea surface temperature. *J. Climate,* **16,** 1441–1455.

Lau, K.-M., C.-H. Sui, M.-D. Chou, and W.-K. Tao, 1994: An inquiry into the cirrus-cloud thermostat effect for tropical sea surface temperature. *Geophys. Res. Lett.,* **21,** 1157–1160.

Lin, B., B. A. Wielicki, L. H. Chambers, Y. Hu, and K.-M. Xu, 2002: The iris hypothesis: A negative or positive cloud feedback? *J. Climate,* **15,** 3–7.

——, ——, P. Minnis, L. H. Chamber, K.-M. Xu, Y. Hu, and A. Fan, 2006: The effect of environmental conditions on tropical deep convective systems observed from the TRMM satellite. *J. Climate,* **19,** 5745–5761.

Lindzen, R., M.-D. Chou, and A. Hou, 2001: Does the earth have an adaptive infrared iris? *Bull. Amer. Meteor. Soc.,* **82,** 417–432.

Loeb, N. G., N. Manalo-Smith, S. Kato, W. F. Miller, S. K. Gupta, P. Minnis, and B. A. Wielicki, 2003: Angular distribution models for top-of-atmosphere radiative flux estimation from the Clouds and the Earth's Radiant Energy System instrument on the Tropical Rainfall Measuring Mission satellite. Part I: Methodology. *J. Appl. Meteor.,* **42,** 240–265.

Luo, Y., K.-M. Xu, B. A. Wielicki, Z. A. Eitzen, and T. Wong, 2007: Statistical analyses of satellite cloud object data from CERES. Part III: Comparison with cloud-resolving model simulations of tropical convective clouds. *J. Atmos. Sci.,* in press.

Mace, G. G., Y. Zhang, S. Platnick, M. D. King, P. Minnis, and P. Yang, 2005: Evaluation of cirrus cloud properties derived from MODIS data using cloud properties derived from ground-based observations collected at the ARM SGP site. *J. Appl. Meteor.,* **44,** 221–240.

Minnis, P., and Coauthors, 1997: Cloud optical property retrieval (Subsystem 4.3). Clouds and the Earth's Radiant Energy System (CERES) algorithm theoretical basis document. Volume III: Cloud analyses and radiance inversions (Subsystem 4), CERES Science Team, Eds., NASA, 60 pp. [Available online at http://asd-www.larc.nasa.gov/ATBD/ATBD.html.]

Mishchenko, M. I., W. B. Rossow, A. Macke, and A. A. Lacis, 1996: Sensitivity of cirrus cloud albedo, bidirectional reflectance and optical thickness retrieval accuracy to ice particle shape. *J. Geophys. Res.,* **101,** 16 973–16 985.

Ohring, G., B. A. Wielicki, R. Spencer, B. Emery, and R. Datla, 2005: Satellite instrument calibration for measuring global climate change: Report of a workshop. *Bull. Amer. Meteor. Soc.,* **86,** 1303–1313.

Ramanathan, V., and W. Collins, 1991: Thermodynamic regulation of ocean warming by cirrus clouds deduced from observations of the 1987 El Niño. *Nature,* **351,** 27–32.

Reynolds, R. W., and T. M. Smith, 1994: Improved global sea surface temperature analyses using optimum interpolation. *J. Climate,* **7,** 929–948.

Schlesinger, M. E., 1985: Feedback analysis of results from energy balance and radiative-convective models. *Projecting the Climatic Effects of Increasing Carbon Dioxide,* M. C. MacCracken and F. M. Luther, Eds., U.S. Department of Energy, 280–319.

Solman, S. A., and C. G. Menéndez, 2002: ENSO-related variability of the Southern Hemisphere winter storm track over the eastern Pacific–Atlantic sector. *J. Atmos. Sci.,* **59,** 2128–2140.

Wielicki, B. A., and R. M. Welch, 1986: Cumulus cloud properties derived using Landsat satellite data. *J. Climate Appl. Meteor.,* **25,** 261–276.

——, R. D. Cess, M. D. King, D. A. Randall, and E. E. Harrison, 1995: Mission to planet Earth: Role of clouds and radiation in climate. *Bull. Amer. Meteor. Soc.,* **76,** 2125–2153.

——, B. R. Barkstrom, E. F. Harrison, R. B. Lee III, G. L. Smith, and J. E. Cooper, 1996: Clouds and the Earth's Radiant Energy System (CERES): An Earth Observing System Experiment. *Bull. Amer. Meteor. Soc.,* **77,** 853–868.

Xu, K.-M., 2006: Applying the bootstrap method for statistical significance test of differences between histograms. *Mon. Wea. Rev.,* **134,** 1442–1453.

——, and D. A. Randall, 1995: Impact of interactive radiative transfer on the macroscopic behavior of cumulus ensembles. Part II: Mechanisms for cloud-radiation interactions. *J. Atmos. Sci.,* **52,** 800–817.

——, T. Wong, B. A. Wielicki, L. Parker, and Z. A. Eitzen, 2005: Statistical analyses of satellite cloud object data from CERES. Part I: Methodology and preliminary results of 1998 El Niño/2000 La Niña. *J. Climate,* **18,** 2497–2514.